
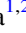

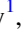

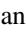







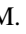

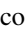
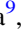


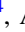
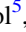





Prompt Emission and Early Optical Afterglow of Very-high-energy Detected GRB 201015A and GRB 201216C: Onset of the External Forward Shock

Amit Kumar Ror¹ , Rahul Gupta^{1,2} , Martin Jelínek³ , Shashi Bhushan Pandey¹ , A. J. Castro-Tirado^{4,5} , Y.-D. Hu⁴ , Alžběta Maleňáková³ , Jan Štrobl³ , Christina C. Thöne³ , René Hudec³ , Sergey Karpov⁶ , Amit Kumar^{1,7} , A. Aryan^{1,2} , S. R. Oates⁸ , E. Fernández-García⁴ , C. Pérez del Pulgar⁵ , M. D. Caballero-García⁴ , A. Castellón⁹ , I. M. Carrasco-García⁹ , I. Pérez-García⁴ , A. J. Reina Terol⁵ , and F. Rendon⁴ 

¹ Aryabhata Research Institute of Observational Sciences (ARIES), Manora Peak, Nainital-263002, India; amitror@aries.res.in, rahulbhu.c157@gmail.com, shashi@aries.res.in

² Department of Physics, Deen Dayal Upadhyaya Gorakhpur University, Gorakhpur-273009, India

³ Astronomical Institute of the Czech Academy of Sciences (ASU-CAS), Fričova 298, 251 65 Ondřejov, Czech Republic

⁴ Instituto de Astrofísica de Andalucía (IAA-CSIC), Glorieta de la Astronomía s/n, E-18008, Granada, Spain

⁵ Unidad Asociada al CSIC Departamento de Ingeniería de Sistemas y Automática, Escuela de Ingenierías, Universidad de Málaga, C. Dr. Ortiz Ramos sn, E-29071, Málaga, Spain

⁶ Institute of Physics of the Czech Academy of Sciences (FZU AV ČR), Na Slovance 2, Praha 8, Czech Republic

⁷ Department of Physics, University of Warwick, Gibbet Hill Road, Coventry CV4 7AL, UK

⁸ School of Physics and Astronomy & Institute for Gravitational Wave Astronomy, University of Birmingham, B15 2TT, UK

⁹ Facultad de Ciencias, Universidad de Málaga, E-29010 Málaga, Spain

Received 2022 October 2; revised 2022 November 17; accepted 2022 November 17; published 2023 January 4

Abstract

We present a detailed prompt emission and early optical afterglow analysis of the two very-high-energy (VHE) detected bursts GRB 201015A and GRB 201216C, and their comparison with a subset of similar bursts. Time-resolved spectral analysis of multistructured GRB 201216C using the Bayesian binning algorithm revealed that during the entire duration of the burst, the low-energy spectral index (α_{pt}) remained below the limit of the synchrotron line of death. However, statistically some of the bins supported the additional thermal component. Additionally, the evolution of spectral parameters showed that both the peak energy (E_p) and α_{pt} tracked the flux. These results were further strengthened using the values of the physical parameters obtained by synchrotron modeling of the data. Our earliest optical observations of both bursts using the F/Photometric Robotic Atmospheric Monitor Observatorio del Roque de los Muchachos and Burst Observer and Optical Transient Exploring System robotic telescopes displayed a smooth bump in their early optical light curves, consistent with the onset of the afterglow due to synchrotron emission from an external forward shock. Using the observed optical peak, we constrained the initial bulk Lorentz factors of GRB 201015A and GRB 201216C to $\Gamma_0 = 204$ and $\Gamma_0 = 310$, respectively. The present early optical observations are the earliest known observations constraining outflow parameters and our analysis indicate that VHE detected bursts could have a diverse range of observed luminosity within the detectable redshift range of present VHE facilities.

Unified Astronomy Thesaurus concepts: [Gamma-ray bursts \(629\)](#)

1. Introduction

Gamma-ray bursts (GRBs) are sudden intense explosions of electromagnetic radiation in the keV–MeV energy range, releasing energy ($E_{\gamma,\text{iso}}$) in the range of 10^{51-54} erg. GRBs emit radiation across the electromagnetic spectrum broadly into two successive phases, i.e., prompt emission (generally in the gamma rays or hard X-ray band) and afterglow emission (from radio to gamma rays), respectively (Kumar & Zhang 2015). These cosmic stellar explosions are traditionally classified into long (LGRBs) and short (SGRBs) depending on their observed prompt-emission duration (Kouveliotou et al. 1993), which can be traced back to different progenitors. A massive star collapse under certain physical conditions, a “collapsar,” is expected to be the progenitor of LGRBs (Woosley 1993; Hjorth et al. 2003). On the other hand, SGRBs are believed to originate from the merging of compact binaries like two neutron stars or a neutron star and a black hole (Perna & Belczynski 2002;

Abbott et al. 2017). However, recent discoveries of a few GRBs exhibiting hybrid properties from the collapse of massive stars (Ahumada et al. 2021) as well as from binary mergers (Rastinejad et al. 2022; Troja et al. 2022) challenge current understanding and provide valuable clues about the physical nature of progenitors of GRBs.

There are many open questions related to the physics behind the prompt emission of GRBs, such as their jet compositions, emission mechanisms, and emission radii (see Kumar & Zhang 2015; Pe’er 2015 for a review). To understand the jet compositions, there are two widely accepted scenarios: (1) baryonic-dominated hot fireball (Shemi & Piran 1990), and (2) Poynting-flux-dominated outflow (Zhang et al. 2018). In addition, there is also the possibility of a hybrid model that includes both components: a Poynting flux outflow moving along with a hot fireball (Pe’er 2015). For the emission mechanisms, there are two widely accepted scenarios: (1) synchrotron emission from a cooling population of particles (Burgess et al. 2020), and (2) thermal photospheric emission (Pe’er 2015). Since the beginning of GRB spectroscopy, prompt spectral analysis of a larger sample of Burst And Transient Source Experiment GRBs suggests nonthermal

dominance, and the spectra are described by a smoothly connected power-law empirical function, known as the Band function (Band et al. 1993). The low-energy spectral index of the Band function is widely used to understand the possible radiation process. However, some authors used the physical synchrotron modeling and suggested that it is a more accurate method to constrain the radiation physics rather than empirical fitting (Oganesyan et al. 2019; Burgess et al. 2020).

Contrary to those predicted within the framework of the external forward and reverse-shock models (Sari et al. 1998; Sari & Piran 1999), the early time broadband afterglow emission of some GRBs exhibit deviations from power-law behavior such as flares, bumps, and plateaus largely attributed to effects from the unknown central engine. The early optical afterglow light curve initially rises until the blast wave reaches the self-similar phase, and the bulk Lorentz factor remains almost constant to its initial value. When the light curve is at its peak, the blast wave carries enough matter for the bulk Lorentz factor to begin progressively decreasing following the self-similar solution (Blandford & McKee 1976), which makes the light-curve decay, a process known as the onset of the afterglow (Sari & Piran 1999). Sari & Piran (1999) explored the early optical afterglow emission and noted that the detection of the onset of the afterglow can be utilized to calculate the initial bulk Lorentz factor of the relativistic outflow. Fast slewing (within a few minutes) of optical space (Swift Ultra-Violet and Optical Telescope) and ground-based telescopes (robotic telescopes such as MASTER, the Burst Observer and Optical Transient Exploring System (BOOTES), the F/Photometric Robotic Atmospheric Monitor (FRAM), etc.) are required to discover the onset of optical afterglow. Liang et al. (2010) carried out an extensive search for the onset signatures in the early afterglow and identified 20 GRBs (through the literature search up to 2009) with an initial bump in their optical light curves. Additionally, they studied correlations among the characteristic parameters of the optical bump, like the peak time, FWHM, and isotropic energy, and noted that most of the parameters have strong correlations with each other.

In recent years, detections of very-high-energy (VHE) gamma-ray emissions during the afterglow phase by the imaging atmospheric Cherenkov telescopes such as Major Atmospheric Gamma Imaging Cherenkov (MAGIC; MAGIC Collaboration et al. 2019a), High Energy Stereoscopic System (HESS; HESS Collaboration et al. 2021), and Large High Altitude Air Shower Observatory (LHAASO; Huang et al. 2022) including the recently discovered GRB 221009A have challenged our understanding of afterglows and has opened a new window to explore this phase in more detail. A few general characteristics of VHE detected GRBs are tabulated in Table 1. Generally, the traditional synchrotron emission cannot explain the spectral energy distributions (SEDs) of VHE detected bursts. The double-bump features observed in the broadband SEDs of GRB 180720B and GRB 190114C demand a synchrotron emission mechanism for the first bump and synchrotron-self Compton (SSC) to account for the second bump (Abdalla et al. 2019; MAGIC Collaboration et al. 2019a). However, in the case of the nearby VHE detected GRB 190829A, the spectral index calculated using HESS data was similar to the one of the synchrotron emission observed in the X-ray band, indicating that a single synchrotron component is sufficient to model the observed broadband spectrum from radio to VHE energies (HESS Collaboration et al. 2021). In addition, in the case of GRB 190829A and GRB 190114C,

dusty environments (large values of optical extinction in the host galaxies) have been observed, indicating a possible relationship between the occurrence of VHE emission and dusty environments (de Ugarte Postigo et al. 2020b; Zhang et al. 2021; Gupta et al. 2022a).

In this paper, we present a detailed prompt emission and early optical afterglow analysis of two of the VHE detected bursts, GRB 201015A (Suda et al. 2022) and GRB 201216C (Fukami et al. 2022). The article has been organized in the following sections: Section 2 presents multiwavelength observations of GRB 201015A and GRB 201216C, followed by the prompt and afterglow data analysis. The main results are given in Section 3, and followed by the discussion in Section 4. Finally, the summary and conclusions are given in Section 5. Unless otherwise stated, the uncertainties are expressed in 1σ throughout this article. We consider the Hubble parameter $H_0 = 71 \text{ km s}^{-1} \text{ Mpc}^{-1}$, and the density parameters $\Omega_\Lambda = 0.73$ and $\Omega_m = 0.27$.

2. Multiwavelength Observations and Data Reduction

In the present section, we report the prompt emission, afterglow observations, and data reduction of GRB 201015A and GRB 201216C taken from space and ground-based facilities and are part of the present analysis.

2.1. Prompt Gamma-Ray Observations

The Burst Alert Telescope (BAT, Barthelmy et al. 2005) on board the Neil Gehrels Swift observatory (henceforth Swift) triggered GRB 201015A at 22:50:13.00 UT on 2020 October 15 (T_0) with a total duration of ~ 10 s in the 15–350 keV energy range. The burst was localized to R.A., decl. = $354^\circ 310$, $+53^\circ 446$ (J2000) with a BAT uncertainty circle of $2'9$ (D’Elia et al. 2020). At the time of Swift detection, the Gamma-ray Burst Monitor (GBM; Meegan et al. 2009) on board Fermi was observing the field of view of the GRB, but was unable to trigger on the burst. However, the burst was identified in GBM data through a targeted search from ± 30 s around the Swift-BAT trigger time.

The Fermi-GBM triggered GRB 201216C at 23:07:25.75 UT on 2020 December 16 (T_0 ; Malacaria et al. 2020). At T_0 , the burst location was outside the field of view (FoV) of the Large Area Telescope (LAT) on board Fermi (boresight angle is $93^\circ 0$). It came into the FoV of LAT at $\sim T_0 + 3500$ s and remained visible until $\sim T_0 + 5500$ s. However, no significant GeV emission associated with GRB 201216C was observed during this time window (Bissaldi et al. 2020). In addition to Fermi, the Swift-BAT triggered GRB 201216C at 23:07:31.00 UT on 2020 December 16 with a T_{90} duration of 48.0 ± 16.0 s in the 15–350 keV range (Beardmore et al. 2020; Ukwatta et al. 2020). The burst was localized at R.A., decl. = $16^\circ 358$, $+16^\circ 537$ (J2000) with a BAT uncertainty circle of radius $3'$ (Beardmore et al. 2020). The prompt emission of GRB 201216C was also detected by AstroSat CZT-Imager (Nadella et al. 2020) and Konus-Wind (Frederiks et al. 2020).

Swift-BAT data analysis: We retrieved the Swift-BAT observation data for both bursts from their Swift archive pages (GRB 201015A, obsID: 01000452000 and GRB 201216C, obsID: 01013243000¹⁰), respectively. We performed general processing of the BAT data given in the Swift-BAT Software

¹⁰ <https://www.swift.ac.uk/archive/selectseq.php?tid=01013243&source=obs>

Table 1
General Characteristics of VHE Detected GRBs

VHE Detected GRBs	Light-curve Morphology	z	E_p (keV)	$E_{\gamma,iso}$ (erg)	$L_{\gamma,iso}$ (erg s $^{-1}$)	Ambient Medium	X-Ray Flare	Supernova Connection
160821B (1), (2)	Short and bright pulse	0.162	84 ± 19	2.10×10^{50}	2.00×10^{50}	ISM	No	kilonova
180720B (3), (4)	Single broad multipeak light curve	0.654	451 ± 49	6.00×10^{53}	1.80×10^{53}	ISM	Yes	No
190114C (5), (6)	Bright multipeak pulse followed by soft tail emission	0.424	926 ± 17	2.50×10^{53}	1.67×10^{53}	wind/ISM	No	Yes
190829A (7), (8)	Two episodes with 40 s quiescent gap	0.0785	11.5 ± 0.4	3.00×10^{50}	3.00×10^{49}	ISM	Yes	Yes
201015A ^{Present work}	Short overlapping pulses followed by soft and weak tail	0.426	41 ± 14	3.86×10^{51}	3.86×10^{50}	ISM	No	Yes
201216C ^{Present work}	Complex multipulsed structured light curve	1.1	352 ± 12	6.32×10^{53}	8.78×10^{52}	wind	No	No
221009A (9), (10), (11), (12), (13)	Two emission episodes followed by a long tail, extraordinarily brightness	0.151	1060 ± 30	$>3 \times 10^{54}$	$>1 \times 10^{52}$	wind	No	Yes

Note. Characteristic properties of the VHE detected GRBs (GRB 160821B has no firm detection; there is evidence of a signal of VHE emission at the level of 3σ) obtained from our analysis along with those published in several papers given below: (1) Lamb et al. (2019), (2) Troja et al. (2019), (3) Fraija et al. (2019b), (4) Huang et al. (2020), (5) MAGIC Collaboration et al. (2019a, 2019b), (6) Fraija et al. (2019a), (7) Fraija et al. (2021), (8) Hu et al. (2021), (9) Dichiara et al. (2022), (10) Huang et al. (2022), (11) Ren et al. (2022), (12) de Ugarte Postigo et al. (2022), (13) Vinko & Wheeler (2022).

Guide.¹¹ Further, we analyzed the standard temporal and spectral BAT data products following the BAT data analysis methods given in Gupta et al. (2021a), Caballero-García et al. (2022). In this work, we have utilized the multimission maximum likelihood framework (Vianello et al. 2015, 3ML¹²) software for the time-averaged spectral analysis. We considered the BAT spectrum over the 15–150 keV energy range for the spectral analysis of the BAT data.

Fermi-GBM data analysis: For the Fermi-GBM data analysis of GRB 201216C, we downloaded the GBM time-tagged events (TTE) mode data from the Fermi-GBM Burst Catalog.¹³ We selected the three brightest sodium iodide (NaI) and brightest bismuth germanate (BGO) detectors with minimum observing angles for temporal and spectral analysis of GBM data. We followed the methodology given in Caballero-García et al. (2022) and Gupta et al. (2022b) for the spectral and temporal analysis of Fermi-GBM data.

In this work, we have utilized the 3ML (Vianello et al. 2015) software for the time-averaged and time-resolved¹⁴ spectral analysis. We considered the GBM spectrum over 8–900 keV (NaI detectors) and 200–40,000 keV (BGO detector) energy ranges. We initially used two empirical models, *Band* and *Cutoff power-law* (CPL), to fit the time-averaged spectrum. To find the best-fit model among the empirical models, we compared the deviance information criterion (DIC) values and chose the best model with the least DIC value ($\Delta \text{DIC} < -10$). Furthermore, we checked whether the addition of a thermal component (*Blackbody*) with *Band*, or *Cutoff power-law* in the spectrum improves the fitting or not. We have applied the following criterion to determine if the spectrum has a thermal component:

$$\Delta \text{DIC}_{\text{Band/CPL}} = \text{DIC}_{\text{Band+BB/CPL+BB}} - \text{DIC}_{\text{Band/CPL}}.$$

The negative value of ΔDIC suggests an improvement in the spectral fit. If the difference in DIC is less than -10 , it shows the existence of a significant amount of thermal component in the spectrum.

Burgess et al. (2020) suggested that the empirical models may not be able to reveal the emission process of GRBs. They found that GRB spectra can be well modeled with a physical synchrotron model even if the low-energy spectral index of the same spectra exceeds the synchrotron line of death if modeled using a *Band* model. Therefore, in addition to empirical models, we have also used the physical synchrotron to model the emission mechanism of GRB 201216C. In this article, we have used the same physical synchrotron model *pynchrotron*¹⁵ (synchrotron emission from cooling electrons) for the spectral modeling of GRB 201216C used in Burgess et al. (2020). The synchrotron model is based on a comprehensive electron acceleration mechanism assumption. According to that, electrons are continuously injected into a power-law spectrum: $N(\gamma) \propto \gamma^{-p}$ with $\gamma_{\text{inj}} \leq \gamma \leq \gamma_{\text{max}}$, where p is the spectral index of the injected electrons, γ_{inj} and γ_{max} are the lower and upper boundaries of the injected electron spectrum, respectively. The cool synchrotron physical model details have

been explained in Burgess et al. (2020). This model is characterized by the six physical parameters: (1) magnetic field strength (B), (2) spectral index of electrons (p), (3) γ_{inj} , (4) γ_{max} , (5) characteristic Lorentz factor corresponds to the electrons' cooling time (γ_{cool}), and (6) bulk Lorentz factor (γ_{bulk}).

During the spectral modeling, we fixed some of the physical parameters. We have fixed $\gamma_{\text{inj}} = 10^5$ due to a strong degeneracy between the magnetic field strength and γ_{inj} . The bulk Lorentz factor (γ_{bulk}) is fixed at 513, obtained using the onset of optical afterglow (see Section 3.2.2). Furthermore, we have fixed $\gamma_{\text{max}} = 10^8$ as the fast-cooling synchrotron physical model does not fit the prompt spectrum of GRBs well (Burgess et al. 2020).

Time-resolved spectral analysis of GRB 201216C: Time-resolved spectral analysis of the prompt emission using broad-spectral-coverage GRB detectors such as Fermi-GBM has been used as a promising tool to investigate the emission mechanism and to study the correlations between the spectral parameters of GRBs. To constrain the radiation process and spectral evolution of GRB 201216C, we performed the time-resolved spectral analysis using the 3ML software with the same number of detectors used for the time-averaged spectral analysis. 3ML provides four possible methods to bin the light curves of GRBs. (1) Constant cadence (Cc) binning: All bins are equally spaced with the initially chosen time width ΔT . One disadvantage is that the spectral shape may vary slower or faster than the specified cadence. (2) Signal-to-noise ratio (S/N) binning: Here, we predefined the S/N for each bin, which ensures enough photons in each time bin, but it may fail to recover the intrinsic spectral evolution behavior of GRBs. (3) Knuth binning. (4) Bayesian blocks binning: In this case, the time bins have unequal widths and a variable S/N. Burgess (2014) studied all these methods and suggested that the Bayesian blocks binning method is the best time-slicing method to correctly obtain the intrinsic spectral evolution of GRBs. However, this method has one limitation: some bins might not have enough photons needed for correct spectral modeling. In the case of GRB 201216C, we initially performed the Bayesian blocks binning on the brightest GBM detector (energy range of 8–900 keV) considering the false-alarm probability $P = 0.01$ (Scargle et al. 2013), and the other GBM detectors used the same temporal binning information. This results in 37 time-sliced spectra for the time-resolved analysis of GRB 201216C. Further, we measured each spectrum's statistical significance (S ; Vianello 2018) to ensure enough photon counts for spectral analysis and considered temporal bins with statistical significance greater than 25. This results in 27 time-sliced (Bayesian blocks) spectra with $S > 25$.

For the time-resolved spectral analysis of GRB 201216C, we initially used the empirical *Band* and *Cutoff power-law* models and then refitted each spectrum after adding a thermal component to the empirical models. Furthermore, we fitted each spectrum using the physical slow-cooling *Synchrotron* model. We have used the Bayesian fitting method for the spectral fitting, and the sampler is set to the *multi-nest* with 10,000 iterations. The spectral parameters, along with the associated errors, obtained using the time-resolved spectral analysis of GRB 201216C using the empirical and physical models are given in Tables B2, B3, and B4 of the Appendix.

¹¹ https://swift.gsfc.nasa.gov/analysis/bat_swguide_v6_3.pdf

¹² <https://three.ml.readthedocs.io/en/latest/>

¹³ <https://heasarc.gsfc.nasa.gov/W3Browse/fermi/fermigbrst.html>

¹⁴ For GRB 201015A, we could not perform the time-resolved spectral analysis as Fermi (having broad spectral coverage) was unable to trigger on the burst.

¹⁵ <https://github.com/grburgess/pynchrotron>

2.2. Afterglow Observations

The afterglows of GRB 201015A¹⁶ and GRB 201216C¹⁷ were discovered from VHE to radio wavelengths by various observational facilities over the globe, including our earliest optical afterglow observations using the robotic telescopes, FRAM Observatorio del Roque de los Muchachos (ORM; Jelinek et al. 2020a, 2020b) and BOOTES (Hu et al. 2020). The redshifts of GRB 201015A ($z = 0.426$) and GRB 201216C ($z = 1.1$) were measured using spectroscopic observations (emission features) of 10.4 m GTC (de Ugarte Postigo et al. 2020a) and the Very Large Telescope (VLT; Vielfaure et al. 2020), respectively. The redshift measurement of GRB 201216C places the burst as the most distant known source associated with VHE emission (see Table 1).

2.2.1. X-Ray Afterglows

For GRB 201015A, Swift could not slew until $T_0 + 51.6$ minutes due to an observing constraint (D’Elia et al. 2020). The Swift X-ray telescope (XRT; Burrows et al. 2005) began observations of GRB 201015A at 23:43:47.2 UT on 2020 October 15, ~ 3214.1 s post burst. Swift-XRT detected an uncatalogued fading X-ray source at the following location: R.A., decl. = 354°32067, +53°41460 (J2000) with an uncertainty radius of 3'8 (Kennea et al. 2020). Swift-XRT observed this source up to $\sim 1.8 \times 10^3$ ks after the BAT detection. All observations were obtained in the photon counting (PC) mode.

For GRB 201216C, Swift-XRT began observations at 23:56:58.5 UT on 2020 December 16, ~ 2966.8 s post burst. Swift-XRT detected a new fading X-ray source at the following location: R.A., decl. = 16°37114, +16°51659 (J2000) with an uncertainty circle of 3'5 (Campana et al. 2020). Swift-XRT observed this source up to 2.2×10^3 ks after the initial detection. The window timing (WT) mode was used for the first ~ 25 s of observations, and the remaining observations were obtained in the PC mode.

X-ray afterglow data analysis: In this work, we obtained the Swift-XRT data products from the XRT repository provided by the University of Leicester (Evans et al. 2007, 2009). We modeled the X-ray afterglow light curves of both bursts using power-law and broken-power-law empirical models to constrain their decay rates. On the other hand, to constrain the spectral indices, we modeled the XRT spectra of both bursts in the energy range of 0.3–10 keV using the X-ray Spectral Fitting Package (XSPEC; Arnaud 1996). We fixed the Galactic hydrogen column density to be $N_{\text{H,Gal}} = 3.60 \times 10^{21}$, and $5.04 \times 10^{20} \text{ cm}^{-2}$ for GRB 201015A and GRB 201216C, respectively (Willingale et al. 2013). A more detailed method for the standard temporal and spectral XRT analysis is given in Gupta et al. (2021a).

2.2.2. Optical Afterglows of GRB 201015A and GRB 201216C

GRB 201015A: The optical afterglow of GRB 201015A was first reported by the MASTER robotic telescope at the position R.A. = 23:37:16.42, decl. = +53:24:55.8 (Lipunov et al. 2020). In this paper, we present our optical observations from the 25 cm FRAM-ORM (Jelinek et al. 2020a), BOOTES (Hu et al. 2020), and 3.6 m Devasthal Optical Telescope (DOT), along with additional optical data from the GCN circulars. Our

photometric observations are listed in Table B8 of the Appendix.

BOOTES-network: The BOOTES-network followed GRB 201015A with three robotic telescopes at the BOOTES-1 (INTA-CEDEA) station in Mazagon (Huelva, Spain) and the BOOTES-2/TELMA station in La Mayora (Malaga, Spain). The BOOTES-1B performed one epoch of early observations at 22:50:48 on 2020 October 15, and the afterglow is clearly seen in the images. The BOOTES-1A performed two epoch observations: the first was the quick follow-up to the trigger, and the second was the late follow-up on the next day. The BOOTES-2/TELMA also followed this event on 2020-10-16T22:15:13. The afterglow was not visible in both BOOTES-1A’s and BOOTES-2’s images.

A series of images were obtained with the BOOTES-1B robotic telescope in the clear filter with exposures of 1, 10, and 60 s for GRB 201015A. The image preprocessing (bias and dark-subtracted, flat-fielded, and cosmic-ray removal) was done using custom IRAF routines. The photometry was carried out using the standard IRAF package. The images were calibrated with nearby comparison stars from the Panoramic Survey Telescope And Rapid Response System (Pan-STARRS) catalog, which were imputed to the R band through the transformation equation¹⁸ for the data in the clear filter. The obtained magnitudes are listed in Table B8 of the Appendix.

FRAM-ORM: The FRAM-ORM is a 25 cm $f/6.3$ robotic telescope facilitated with B , V , R , and z filters and a custom Moravian Instruments G2-1000B1 camera based on a back-illuminated CCD47-10 chip. We carried out the earliest optical observations of GRB 201015A using the 25 cm FRAM-ORM robotic telescope located at La Palma, Spain. We obtained a series of frames with exposure times of 20 s each in the clear filter, beginning on 2020 October 15 at 22:50:50.8 UT (37.6 s after the BAT trigger). We have clearly identified the source mentioned by Lipunov et al. (2020). A finding chart of FRAM-ORM observation of GRB 201015A is given in Figure 1.

3.6 m DOT: We performed the optical observations of the afterglow of GRB 201015A starting on 2020 October 16 at 13:09:07.2 UT (~ 0.6 day post burst) using 3.6 m DOT located at the Devasthal observatory, which is part of the Aryabhata Research Institute of Observational Sciences (ARIES), India. We acquired multiple frames in the B , V , R , and I filters (with an exposure time of 10 minutes in each) using the 4K \times 4K CCD IMAGER (Kumar et al. 2022b) mounted on the main port of 3.6 m DOT. In stacked DOT images, we clearly detect the optical afterglow of GRB 201015A consistent with the error region of NOT observations Malesani et al. (2020). A finding chart of 3.6 m DOT observation of GRB 201015A is given in Figure A8 of the Appendix. We performed the DOT image reduction using the IRAF package. We first applied zero correction and flat-fielding to the raw images taken from the telescope. After the removal of cosmic-ray hits, we stack the images to create a single image. We use the IRAF package to perform the aperture photometry. For the photometric calibration of GRB 201015A, standard stars in the Landolt standard field PG 0231 were observed along with the GRB field in the UBVR bands. The R -band finding chart of GRB 201015A and the secondary stars marked with S1–S14 are shown in Figure A8. The calibrated magnitudes of secondary stars are listed in Table B7 of the Appendix, and the calibrated

¹⁶ <https://gcn.gsfc.nasa.gov/other/201015A.gcn3>

¹⁷ <https://gcn.gsfc.nasa.gov/other/201216C.gcn3>

¹⁸ <http://www.sdss.org/dr12/algorithms/sdssUBVRITransform/>

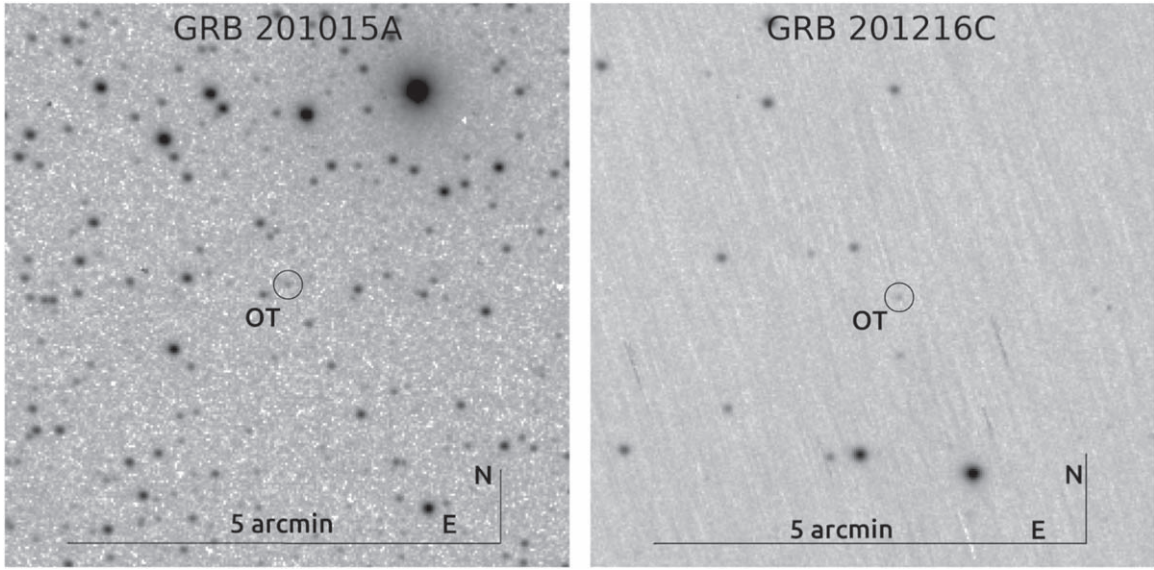


Figure 1. Finding charts of GRB 201015A (left), and GRB 201216C (right) observed utilizing the FRAM-ORM robotic telescope. Circles denote the positions of bursts. The horizontal and vertical lines indicate the directions (north and east). The images have a FoV of $5' \times 5'$.

magnitudes of GRB 201015A are listed in Table B8 of the Appendix.

GRB 201216C: In the case of GRB 201216C, Izzo et al. (2020) carried out the optical follow-up observations in the Sloan g' , r' , z' filters using the VLT telescope, starting at 01:18:47 UT on 2020 December 17. They first reported the detection of an uncatalogued optical source at location R.A.: 01:05:28.980, decl.: +16:31:00.0 (J2000.0), consistent with the Swift-XRT enhanced location (Campana et al. 2020).

FRAM-ORM: We performed the earliest optical follow-up observations to the alert of GRB 201216C using the FRAM-ORM telescope. We obtained a series of frames with an exposure times of 20 s each in the clear filter, starting on 2020 December 16 at 23:08:04.3 UT (31.6 s after the BAT trigger; Jelinek et al. 2020b). We immediately detected an optical transient consistent with the location reported by Izzo et al. (2020). A finding chart of FRAM-ORM observation of GRB 201216C is given in Figure 1. A log of photometric observations of the afterglow of GRB 201216C is presented in Table B9 of the Appendix.

The observed frames for both bursts have been processed through a difference imaging pipeline based on the HOT-PANTS image subtraction code to remove the influence of nearby stars on the photometric measurements and then corrected for bias, flats, and cosmic rays. The photometry has been carried out using the DAOPHOT package. The measured magnitudes have been calibrated using field stars in the Pan-STARRS data release 1 catalog. Our optical observations reveal an early rise in the light curves of both bursts, reaching their maximum and followed by normal decay until the end of our observations. A log of our photometric observations is given in Table B8 of the Appendix.

3. Results

3.1. Prompt Emission

In this section, we present the results of comprehensive analysis of the prompt emission of GRB 201015A and GRB 201216C. We have summarized our results in Table 2.

Table 2

Observed Properties of GRB 201015A and GRB 201216C Obtained from our Comprehensive Analysis of Prompt Emission, Afterglow, and those Reported on GCN Circulars (Malacaria et al. 2020; Markwardt et al. 2020)

Properties	GRB 201015A	GRB 201216C
T_{90} (s)	9.78 ± 3.47	29.95 ± 0.57
HR	0.72	1.11
α_{pt}		-1.06 ± 0.13
β_{pt}	-2.43 ± 0.25	-2.75 ± 0.33
E_p (keV)	$41.37^{+15.74}_{-11.41}$	$352.31^{+13.77}_{-12.74}$
Fluence (erg cm^{-2})	$2.25 \pm 0.38 \times 10^{-7}$	$2.00 \pm 0.10 \times 10^{-4}$
$E_{\gamma,iso}$ (erg)	3.86×10^{51}	6.32×10^{53}
$L_{\gamma,iso}$ (erg s^{-1})	3.86×10^{50}	8.78×10^{52}
Γ_0	~ 204	~ 310
z	0.426	1.1
SN association	Yes	No

Note. The parameters listed in the first column have their standard meaning.

3.1.1. Light Curve and Time-averaged Spectra

The Swift-BAT energy-resolved mask-weighted light curve of GRB 201015A along with HR evolution in 25–50 keV and 50–100 keV energy range is shown in the top panel of Figure 2. The Swift-BAT prompt emission light curve of GRB 201015A has a short-soft emission starting from T_0 and ending at $T_0 + 1$ s, followed by a weak-soft tail emission that lasts until $\sim T_0 + 10$ s (Markwardt et al. 2020). The time-integrated spectrum ($T_0 - 0.21$ to $T_0 + 11.57$ s) of GRB 201015A is explained using the simple power-law model with power index = -2.43 ± 0.25 (see Figure A1 of the Appendix).

The background-subtracted energy-resolved Fermi-GBM light curve of GRB 201216C along with the hardness ratio (HR) evolution is shown in the bottom panel of Figure 2. The Fermi-GBM prompt emission light curve consists of a broad, structured peak with a T_{90} duration of ~ 29.9 s (in 50–300 keV). Similar to the Fermi-GBM observations, Swift-BAT observations also reveal multiple peaks in the mask-weighted prompt light curve. According to BAT observations, the energy fluence of the burst is $4.5 \pm 0.1 \times 10^{-5}$ erg cm^{-2} in the 15–150 keV

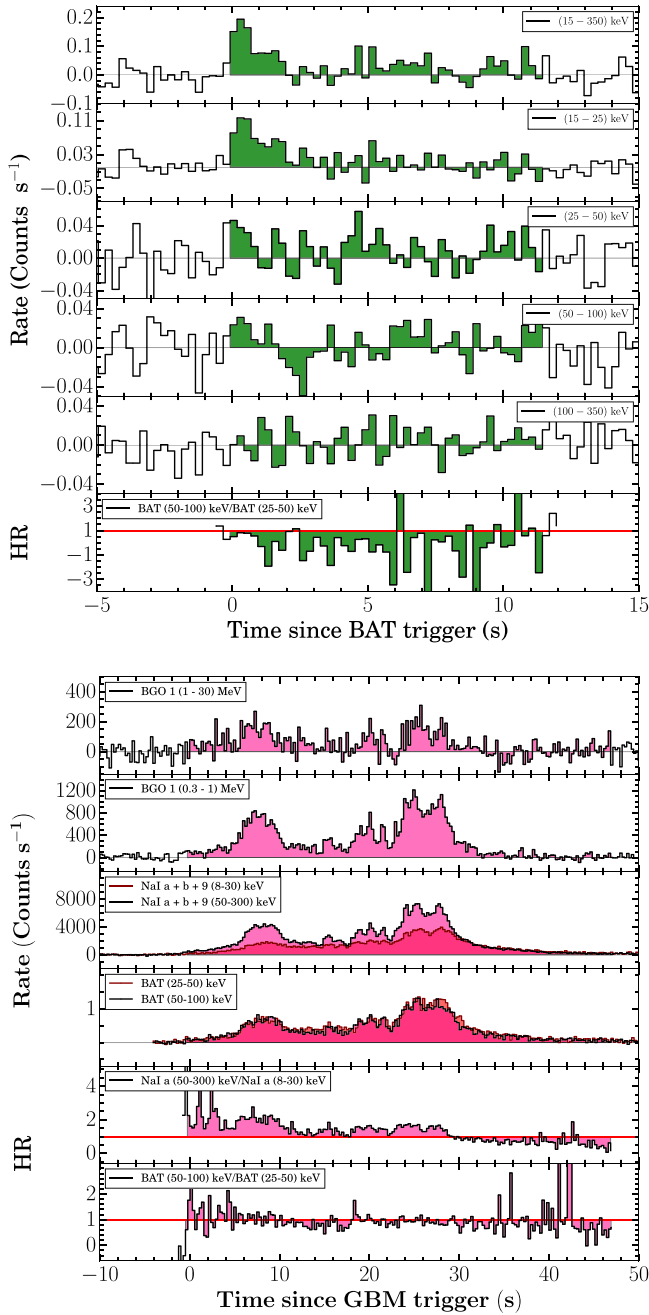


Figure 2. Multichannel prompt γ -ray/hard X-ray light curves of GRB 201015A (top) and GRB 201216C (bottom) along with hardness ratio evolution using Fermi-GBM and Swift-BAT observations. The shaded green and pink regions show the total time interval used for the time-averaged spectral analysis of GRB 201015A and GRB 201216C, respectively.

energy range (Ukwatta et al. 2020). Figure 2 also shows the time interval used for the time-averaged spectral analysis. The time-averaged Fermi-GBM spectrum (from $T_0 - 0.503$ s to $T_0 + 47.09$ s) is best modeled using a Band+BB function (see Figure A1 of the Appendix), and the best-fit spectral parameters are presented in Table B1 of the Appendix. The burst was significantly bright: the observed fluence is $(2.00 \pm 0.10) \times 10^{-4}$ erg cm⁻² in the 10–10⁴ keV energy band over the time-averaged interval. This fluence value is among the top 2% of the brightest GRBs observed by Fermi-GBM. A comparison between the time-averaged energy spectrum of the

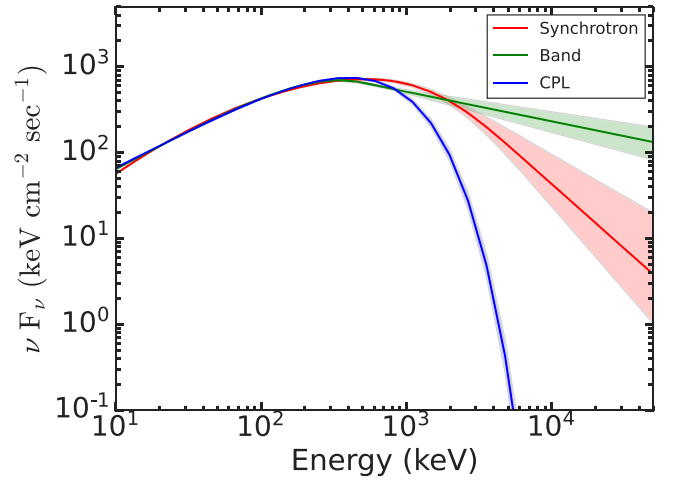


Figure 3. Comparison between the time-averaged energy spectrum of empirical (Band, CPL) and physical (Synchrotron) models for GRB 201216C. The red, green, and blue solid lines show the energy spectrum of the Synchrotron, Band, and Cutoff power-law models in the model space, respectively. The corresponding shaded regions show the 95% confidence interval.

empirical (Band, CPL) and physical (Synchrotron) models are shown in Figure 3.

3.1.2. Time-integrated T_{90} -spectral Hardness Distribution

GRBs are classified into two families based on T_{90} duration; however, there is one more fundamental difference between both classes, i.e., the spectral hardness. Long GRBs are expected to be softer (lower E_p value); on the other hand, short bursts are usually harder (higher E_p value). To know the true class of GRB 201015A and GRB 201216C, we placed both bursts in the time-integrated T_{90} -spectral hardness plane along with the other long and short GRBs obtained from the Fermi-GBM and Swift-BAT catalogs.

We calculated the HR for GRB 201015A using the ratio of fluence in the hard (50–100 keV) and soft (25–50 keV) energy ranges and found its value equal to 0.72. Comparing the HR of GRB 201015A with the Swift-BAT catalog, we note that GRB 201015A is one of the softest bursts ever observed by the Swift mission (see Figure A2 of the Appendix). In the case of GRB 201216C, we calculated the HR using the ratio of counts in the hard (50–300 keV) and soft (8–30 keV) energy ranges to be 1.11, this feature is similar to long/soft GRBs. The distribution of HR as a function of T_{90} for both bursts are given in Figure A2 of the Appendix.

Furthermore, we also placed both bursts in the time-integrated E_p - T_{90} distribution of long and short GRBs. As for GRB 201015A there was no onboard observation by Fermi, and no public Fermi data are available for ground-targeted search; therefore, we have used Swift-BAT observations of GRB 201015A to constrain the time-integrated peak energy. However, the BAT time-integrated spectra of GRBs are usually modeled by simple power-law functions due to the instrument limited spectral coverage (15–150 keV). In the case of GRB 201015A, the time-integrated spectrum is also fitted using a power-law function (see Section 3.1.1). We estimated the E_p value using the known correlation between the Swift-BAT fluence and time-integrated E_p (Zhang et al. 2020), i.e., $E_p = [\text{fluence}/(10^{-5} \text{ erg cm}^{-2})]^{0.28} \times 117.5^{+44.7}_{-32.4}$ keV $\approx 41.37^{+15.74}_{-11.41}$ keV. The estimated time-integrated E_p value of GRB 201015A is consistent with those observed for long GRBs. In the case of GRB 201216C, we fitted the

time-integrated spectrum and calculated the peak energy ($E_p = 352.31^{+12.77}_{-12.74}$ keV) using the best-fit model. The T_{90} - E_p distribution for both GRBs is shown in Figure A2 of the Appendix along with other data points obtained from the Fermi-GBM catalog (Goldstein et al. 2017). We fitted the complete distribution obtained from the Fermi-GBM catalog using the Bayesian Gaussian mixture model (BGMM) algorithm and calculated the probability of GRB 201216C being a long burst as 98.8%.

3.1.3. Prompt Correlations: Amati and Yonetoku

The cosmological corrected time-integrated peak energy $E_{p,z} = (1+z)E_p$ of the prompt emission is correlated with the isotropic equivalent energy $E_{\gamma,iso}$, and isotropic peak luminosity $L_{\gamma,iso}$. The former is known as Amati correlation (Amati 2006), and the later is known as Yonetoku correlation (Yonetoku et al. 2004). In the case of GRB 201015A, we have used Equation (6) of Fong et al. (2015) to calculate $E_{\gamma,iso}$ due to the limitation of Swift-BAT spectral coverage. On the other hand, we have used the best-fit Fermi-GBM time-integrated spectral model to calculate $E_{\gamma,iso}$ for GRB 201216C. The Amati correlation for both GRBs along with a sample of long and short GRBs taken from Minaev & Pozanenko (2020) is presented in Figure A2 of the Appendix. Similarly, we calculated the $L_{\gamma,iso}$ values and placed GRB 201015A and GRB 201216C in the $E_{p,z}$ - $L_{\gamma,iso}$ plane, as shown in Figure A2 of the Appendix. We noticed that both bursts satisfied the Amati and Yonetoku correlations. The calculated isotropic equivalent luminosity values for both bursts suggest that GRB 201015A is an intermediate luminous GRB; on the other hand, GRB 201216C is a luminous GRB.

3.1.4. Time-resolved Spectroscopy of GRB 201216C

Distribution of spectral parameters: The mean values and standard deviation for each spectral parameter obtained using the Cutoff power-law, Band, Cutoff power-law + BB, Band+ BB and Synchrotron models are listed in Table B5 of the Appendix. The mean values of the low-energy spectral indices α_{CPL} obtained using Cutoff power-law and α_{pt} obtained using the Band spectral modeling of GRB 201216C are -1.10 ± 0.14 and -1.06 ± 0.13 , respectively. These values are consistent with the typical average value of the low-energy spectral index ($\alpha_{pt} \sim -1$) of GRBs (Preece et al. 2000). Similarly, the averaged value of spectral peak energy E_p and high-energy photon index β_{pt} obtained using Band are 339.43 ± 119.39 keV, and -2.75 ± 0.33 , respectively. These values are also consistent with the typical average value of E_p and β_{pt} of GRBs. The averaged values of the physical synchrotron spectral parameters for GRB 201216C are as follows: magnetic field (B) = 96.00 ± 45.82 G, index (p) = 4.18 ± 0.54 , and Lorentz factor corresponding to the electron's cooling time $\gamma_{cool} = (6.08 \pm 4.81) \times 10^5$.

Evidence of thermal component: In our time-resolved spectral analysis, we first fitted each binned spectra using empirical Band and Cutoff power-law models individually. To search for the presence of an additional thermal component in the spectrum, we added the Blackbody model along with the Band and Cutoff power-law models, and

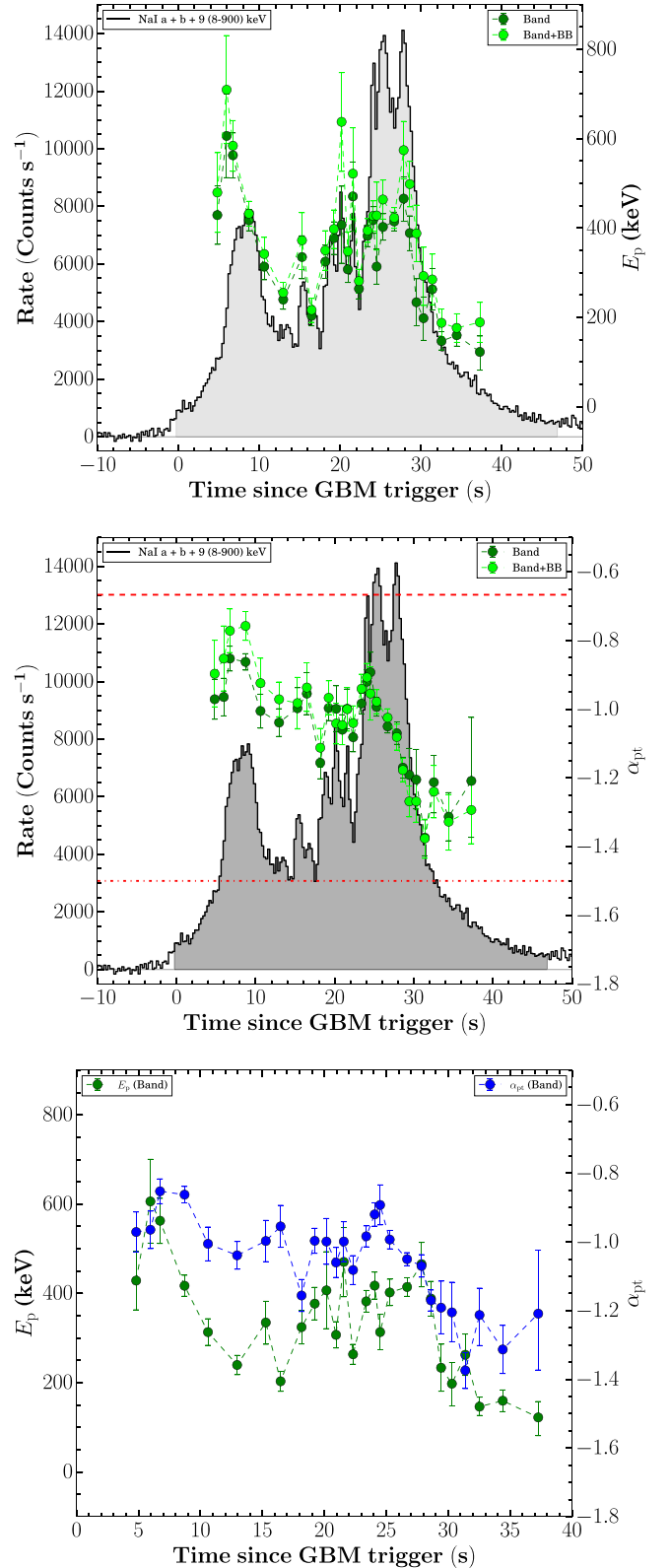


Figure 4. Evolution of the spectral parameters obtained from fitting the Band function. Top panel: evolution of E_p obtained from the Band (dark-green) and Band + Blackbody (green) functions along with the count-rate light curve. Middle panel: same as top panel but for α_{pt} ; the two red dotted lines represent the synchrotron death lines at $-2/3$ and $-3/2$. Bottom panel: comparison of the evolution of E_p (green) and α_{pt} (blue) with time.

calculated the difference of the DIC values. Negative values of $\Delta\text{DIC}_{\text{Band}}$ and $\Delta\text{DIC}_{\text{CPL}}$ imply that the additional `Blackbody` component improves the fit statistic. Furthermore, in the case of any particular bin, $\Delta\text{DIC} < -10$ suggests a significant amount of thermal component present in that particular bin. Figure A3 of the Appendix shows the evolution of ΔDIC within the burst interval for the `Band + Blackbody` model. For all the bins (except the last bin), ΔDIC values are negative, indicating that the addition of thermal components improves the spectral fitting. There are 10 bins ($\sim 37\%$) for which $\Delta\text{DIC} < -10$, suggesting the presence of a thermal component in the spectrum. In light of this, we suggest that GRB 201216C is a hybrid (nonthermal+ quasi-thermal) burst. The thermal components are dominating during the initial and bright phases of the burst.

Evolution of spectral parameters: Studies on the spectral evolution are a very powerful tool to probe the emission process responsible for the prompt emission. The peak energy of the `Band` function shows four different possible types of spectral evolution: (1) the hard-to-soft pattern (Norris et al. 1986), (2) the soft-to-hard pattern (Kargatis et al. 1994), (3) the flux-tracking pattern (Golenetskii et al. 1983), and (4) the chaotic pattern. On the other hand, the low-energy spectral index of the `Band` function also changes with time; however, it does not show any particular trend. There are some recent studies suggesting a flux-tracking pattern of α_{pt} , supporting the double-tracking trend (Li et al. 2019). However, most of the spectral evolution studies are performed for single pulsed bursts. The prompt light curve of GRB 201216C shows a more complex multipulsed structure, and the evolution of the empirical and physical spectral parameters are very interesting. Figure 4 shows the evolution of the spectral parameters (E_p , and α_{pt}) of GRB 201216C obtained using the empirical `Band` function. The evolution of E_p of GRB 201216C shows a flux-tracking trend, i.e., E_p increases and decreases as the flux increases and decreases in respective bins. We noticed that the α_{pt} values are changing with time and do not exceed the expected values of spectral indices of the synchrotron fast- and slow-cooling cases. We have also shown the evolution of α_{pt} and E_p together in Figure 4, and we can see that the evolution patterns are quite similar throughout the emission. Next, we study the spectral evolution of the parameters obtained from the physical synchrotron modeling. Figure 5 shows the spectral evolution of the magnetic field strength (B) and the spectral index of electrons (p). We noticed that the magnetic field strength is also following the intensity of the burst. We could not confirm the evolution trend of p due to large associated errors. In light of the above, we suggest that the multipulsed GRB 201216C has flux-tracking characteristics. We further investigated the correlation among these spectral parameters.

Spectral parameter correlations: Studying the correlations between the different spectral parameters obtained using the time-resolved spectral analysis using empirical and physical modeling gives an important clue about the physics of GRBs and jet composition. We calculated the correlation between the `Band` and `Band+Blackbody` spectral parameters: $\log(\text{flux})$ and $\log(E_p)$, $\log(\text{flux})$ and α_{pt} , $\log(E_p)$ and α_{pt} , and $\log(\text{flux})$ and kT . We found a high degree (the correlation coefficient ranges from 0.60 to 0.79) of correlation between the `Band` spectral parameters, i.e., $\log(\text{flux})$ and $\log(E_p)$, $\log(\text{flux})$ and α_{pt} , and $\log(E_p)$ and α_{pt} . We also found a high degree of correlation between $\log(\text{flux})$ and kT for the `Band+`

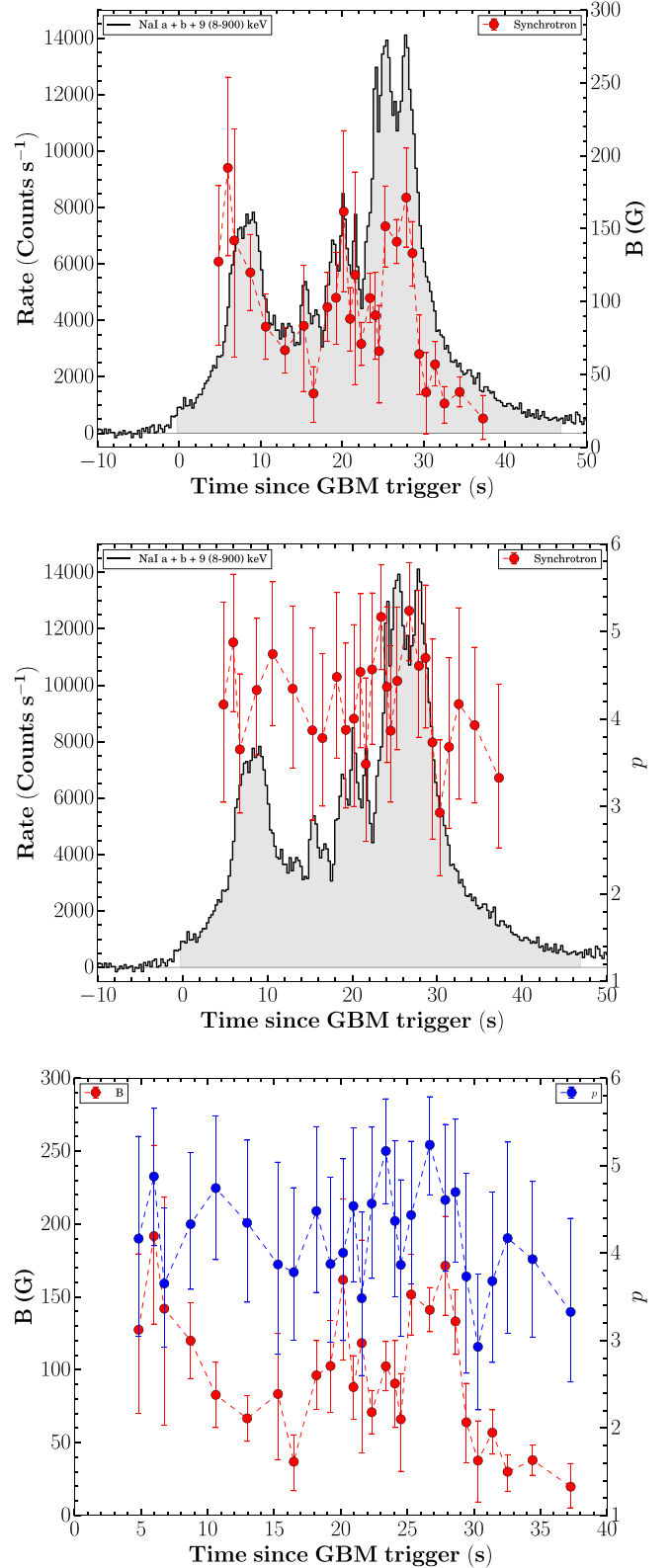


Figure 5. Evolution of the spectral parameters obtained from fitting the physical `Synchrotron` model. Top panel: evolution of the magnetic field strength B along with the count-rate light curve. Middle panel: evolution of the electron energy injection index p along with the count-rate light curve. Bottom panel: comparison of the evolution of B and p with time.

`Blackbody` model. The correlation results for the `Band` and `Band+Blackbody` models (Pearson correlation) are listed in Table B6 and Figure A4 of the Appendix. We also

studied the correlation between the physical spectral parameters ($\log(\text{flux})-\log(B)$, $\log(\text{flux})-p$, and $\log(B)-p$) obtained using the Synchrotron model. We found a very high degree (the correlation coefficient is ≥ 0.80) of correlation between $\log(\text{flux})-\log(B)$ and medium correlation (the correlation coefficient ranges from 0.40 to 0.59) between $\log(B)-p$; however, we found a low degree (the correlation coefficient ranges from 0.20 to 0.39) of correlation between $\log(\text{flux})-p$. The correlation results obtained using physical modeling are shown in Figure A5 and in Table B6 of the Appendix.

In addition, we also studied the correlation between the empirical and physical model parameters: $\log(B)-\log(E_p)$, $\log(B)-\alpha_{\text{pt}}$, and $p-\alpha_{\text{pt}}$. The correlation results are shown in Figure A6 and Table B6 of the Appendix. We found a very high degree of correlation between $\log(B)$ of the physical synchrotron model and $\log(E_p)$ of the empirical Band function. We also found a medium degree of correlation between $\log(B)$ and α_{pt} ; however, there is a low degree of correlation between p and α_{pt} .

3.2. Afterglow Emission of GRB 201015A and GRB 201216C

In the present section, we study the results of the multi-wavelength afterglow of GRB 201015A and GRB 201216C, detected by Swift-XRT (X-ray), FRAM-ORM, BOOTES, and 3.6 m DOT (optical). Multiwavelength light curves of GRB 201015A and GRB 201216C are shown in Figure 6, whereas SEDs are discussed in Figure 7.

3.2.1. X-Ray Afterglows

The X-ray afterglow light curves of GRB 201015A and GRB 201216C do not show any flare, bump, break, or plateau-like activities (see Figure 6).

In the case of GRB 201015A, we initially tried to fit the X-ray light curve using a simple power-law model (temporal index = $-2.36^{+0.17}_{-0.26}$). The calculated XRT temporal index is consistent with the temporal index reported on the XRT catalog page using count-rate light-curve fitting.¹⁹ However, the model shows a significant deviation from the last observed data point ($\chi/\text{dof} = 1.34$). We noted that the last two data points are considered unreliable because no centroid could be determined. We calculated an XRT temporal decay index of $-2.27^{+0.43}_{-0.58}$ excluding these points. We found that both the calculated XRT decay indices are consistent, considering the large associated errors. We also used the broken-power-law function to fit the light curve and obtained $\chi/\text{dof} = 0.27$, indicating that the model is overfitting the data. Further, we used F-test to find the best-fit model among the two empirical models. The F-test suggests that the simple power-law model is better fitting the X-ray afterglow light curve of GRB 201015A, consistent with those reported on the XRT catalog page. The X-ray light curve and the best-fit model are shown in Figure 6. For the XRT spectral analysis, we fitted the late-time spectrum ($T_0 + 4000$ to $T_0 + 22,019$ s) to constrain the intrinsic hydrogen column density (NH_z) of GRB 201015A and calculated $\text{NH}_z = 5.56 \times 10^{21} \text{ cm}^{-2}$. The time-averaged X-ray spectrum ($T_0 + 3300$ to $T_0 + 1,800,000$ s) of GRB 201015A is described using an absorbed-power-law model with a spectral index of $1.10^{+0.25}_{-0.25}$. Further, we divided the XRT light curve into three segments based on available observations. For the first

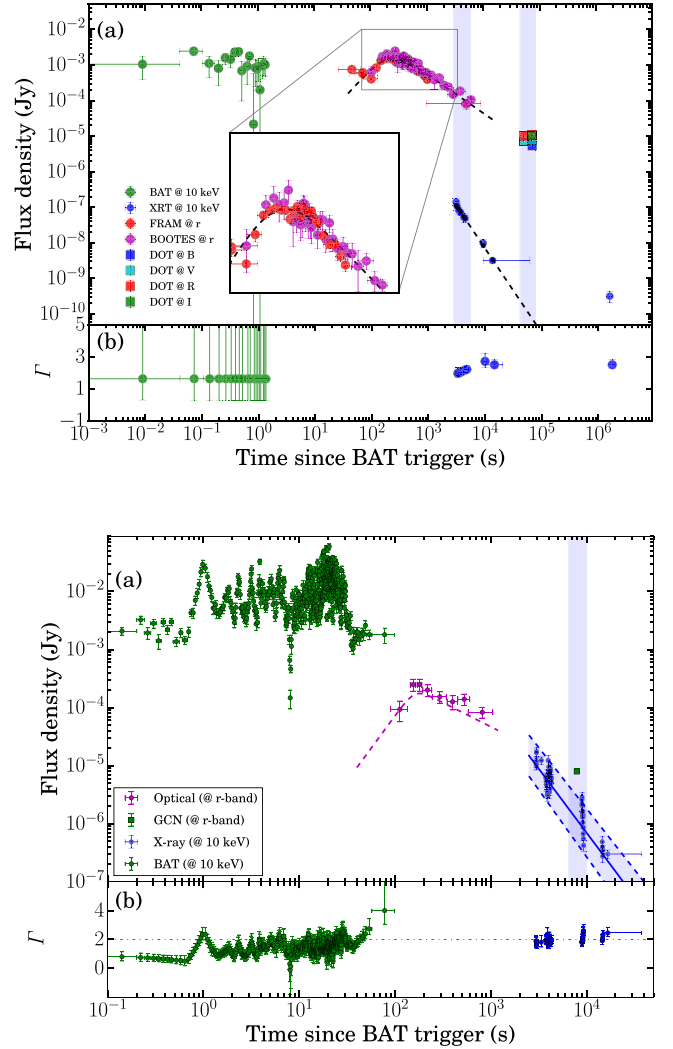


Figure 6. Multiwavelength light curves of GRB 201015A (top) and GRB 201216C (bottom). (a) Swift-BAT (@ 10 keV, green), Swift-XRT (@ 10 keV, blue) and optical (@ r band, red/magenta) flux density light curve. The inset represents the zoomed part of the optical bump. The vertical blue shaded regions indicate the time ranges used for the SED analysis. (b) Evolution of the spectral photon index in the Swift-BAT and Swift-XRT energy channels.

($T_0 + 3300$ to $T_0 + 4800$ s), second ($T_0 + 10,000$ to $T_0 + 15,000$ s), third ($T_0 + 10,000$ to $T_0 + 1,800,000$ s) time bins, we obtained spectral indices of $1.07^{+0.31}_{-0.30}$, $1.10^{+0.53}_{-0.55}$, and $1.38^{+0.49}_{-0.47}$, respectively. Our analysis does not find any noticeable evolution among the spectral indices within the observed duration considering large values of the associated errors.

The X-ray light curve of GRB 201216C is shown in Figure 6. The light curve (@ 10 keV) decays as a power-law with a decay index of $\alpha_x = -2.21^{+0.10}_{-0.11}$ with $\chi/\text{dof} = 3.35$. For the XRT spectral analysis, we calculated the NH_z of the host using the late-time spectral fitting ($T_0 + 4001$ to $T_0 + 37346$ s) and found $\text{NH}_z = 2.71 \times 10^{22} \text{ cm}^{-2}$. The joint PC- and WT-mode time-averaged X-ray spectrum ($T_0 + 2900$ to $T_0 + 17,000$ s) of GRB 201216C is described using an absorbed-power-law model with a spectral index of $0.97^{+0.05}_{-0.05}$. Further, we created the spectrum for individually segmented WT- and PC-mode observations using the Swift Science Data Centre web page²⁰

¹⁹ https://www.swift.ac.uk/xrt_live_cat/01000452/

²⁰ https://www.swift.ac.uk/xrt_spectra/addspec.php?tag=01013243&origin=GRB

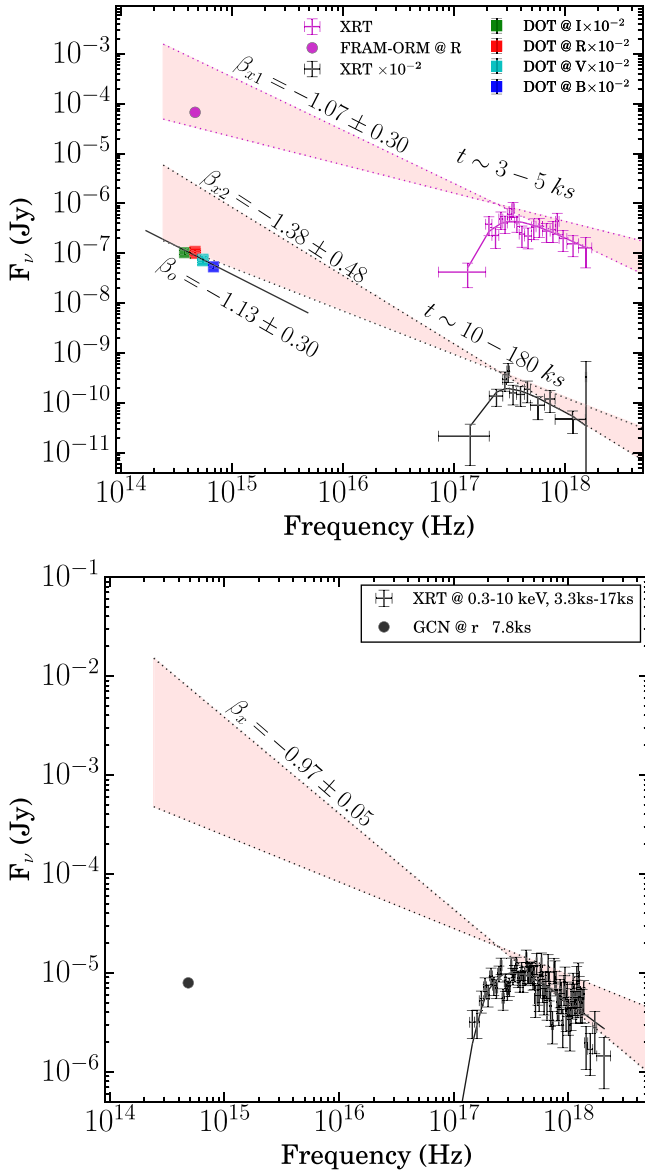


Figure 7. Optical to X-ray SEDs for GRB 201015A and GRB 201216C. Upper panel: SEDs for GRB 201015A at two different epochs; @ 3–5 ks and @ 10–180 ks. The optical data are shown with a filled circle and filled squares at 5 ks and 52–74 ks, respectively, are taken from FRAM-ORM and DOT observations. Data with errors represent the Swift-XRT spectrum (@ 0.3–10 keV). The flux densities at the second epoch are multiplied by 10^{-2} . Lower panel: SEDs for GRB 201216C at 2.9–17 ks from the Swift-BAT trigger time. The filled circle represents the r -band data point taken from GCN circular No. 29066 (Izzo et al. 2020), and the data with errors represent the Swift-XRT spectrum (@ 0.3–10 keV). The pink shaded region represents the range of the predicted synchrotron spectrum $-(p-1)/2 = \beta_x + 0.5$ and $-p/2 = \beta_x$. The optical observations are corrected for Galactic extinction.

and performed the spectral fitting. For the WT ($T_0 + 2900$ to $T_0 + 3000$ s) and PC ($T_0 + 3300$ to $T_0 + 17,000$ s) time bins, we obtained spectral indices of $0.87^{+0.22}_{-0.22}$ and $0.90^{+0.10}_{-0.09}$, respectively. Our analysis indicates that the spectral index does not change with time (see Figure 6).

3.2.2. Optical Afterglows

For both these VHE detected bursts, we can examine the early afterglow behavior using the earliest optical observations from the 0.25 m robotic FRAM-ORM and BOOTES telescopes (Hu et al. 2020; Jelinek et al. 2020a, 2020b).

The optical light curve of GRB 201015A is highly rich in features. Following an early decay, the light curve has a smooth optical bump, which may be either due to reverse-shock emission or the onset of the afterglow in the forward shock. We calculated a decay rate for the very early optical emission of $\alpha_{o1} = -0.68 \pm 0.15$. To characterize the nature of the early bump, we fitted the optical bump using a smoothly broken-power-law function, given in Equation (1)

$$F(t) = F_0 \left[\left(\frac{t}{t_b} \right)^{k\alpha_r} + \left(\frac{t}{t_b} \right)^{k\alpha_d} \right]^{-1/k}, \quad (1)$$

where α_r and α_d are the rise and decay temporal indices, respectively. F_0 is the normalization constant, and t_b is the break time. The break time is related to the observed peak time (t_p) by the following equation:

$$t_p = t_b \left(-\frac{\alpha_r}{\alpha_d} \right)^{[-1/k(\alpha_d - \alpha_r)]}. \quad (2)$$

In the case of GRB 201015A, the smoothly broken-power-law fit (smoothness parameter $k=1$) shows that initially, the optical afterglow light curve rises with a temporal index of $\alpha_r = -1.74^{+0.19}_{-0.23}$ and then decays with an index of $\alpha_d = 1.10^{+0.06}_{-0.06}$, with the break time $t_b = 217.04^{+19}_{-18}$ s post burst. Further, we obtained the peak time $t_p = 184.64^{+17}_{-17}$ s post burst using Equation (2).

In the case of GRB 201216C, our early optical observations with the FRAM-ORM telescope reveals a smooth bump in the optical afterglow light curve. We fitted the optical bump using the smoothly broken-power-law function (see Equation (1)) and calculated the following temporal parameters: rising temporal index $\alpha_r = -0.83^{+0.45}_{-0.41}$, decay temporal index $\alpha_d = 2.24^{+2.14}_{-2.27}$, and break time $t_b = 161.60^{+50}_{-42}$ s post burst, respectively. Further, we determine the peak time $t_p = 179.90^{+50}_{-50}$ s post burst using Equation (2) (smoothness parameter $k=3$).

Reverse shock origin: According to the fireball model, the forward (moving toward the external/surrounding medium) and the reverse (propagating into the blast wave) shocks are originated due to the results of the external shock between the blast wave and ambient medium. The observed early optical peak in the afterglow light curve might be created due to the reverse shock (Kobayashi & Zhang 2003). We used the expected temporal indices (for ISM and wind mediums in the thin- and thick-shell reverse-shock cases) to determine the origin of early optical bump for both bursts (see Table 1 of Gao et al. 2015). We note that the observed temporal indices values during the rising and decaying part of the bump of both bursts are inconsistent with the expected values from the reverse-shock decay in the interstellar medium (ISM) or wind medium. Therefore, the observed early bump in the optical light curves could not be due to the reverse shock.

Onset of optical afterglow: The early peak in the afterglow light curve can be produced by the onset of the afterglow, and it can be used to calculate the bulk Lorentz factor of the fireball (Sari & Piran 1999). Ghirlanda et al. (2018) examined the early temporal coverage of GRBs with a measured redshift and calculated the bulk Lorentz factor for 67 bursts using the peak of the afterglow. In addition, they also summarize the methods used by various authors to estimate the bulk Lorentz factor. In the case of thin-shell regime (T_{90} is less than the deceleration

time), the peak time (in the rest frame) of the light curve provides a direct measurement of the deceleration time t_{dec} . At the deceleration time, the Lorentz factor diminishes by a factor of 2 from its initial value (Γ_0) and enters into the self-similar deceleration phase. For the homogeneous medium surrounding the burst, the thin-shell deceleration time is related to the deceleration radius R_{dec} and bulk Lorentz factor with the following relation (Sari & Piran 1999; Molinari et al. 2007):

$$t_{\text{dec}} = R_{\text{dec}}/2c\Gamma_0^2. \quad (3)$$

Further, Ghirlanda et al. (2018) generalized the relation for both types of the surrounding medium (see Equation (4))

$$\Gamma_0 \sim K \left[\frac{E_{\gamma,\text{iso}}}{nm_p c^{5-s} \eta^{1-s} t_{p,z}^{3-s}} \right]^{\frac{1}{8-2s}}, \quad (4)$$

where $s = 0$ and $K = 1.702$ for ISM, and $s = 2$ and $K = 1.543$ for the wind-like ambient medium. $E_{\gamma,\text{iso}}$ is the isotropic equivalent γ -ray energy, m_p is the proton mass, n is the circumburst medium density, and η is the radiative efficiency of the fireball.

The optical light curves of both GRB 201015A and GRB 201216C have a smooth bump that is well separated from the prompt emission, implying that the emission is in the thin-shell regime. For the present analysis, we consider η equal to 0.2 for both types of ambient medium. Further, we assume the value of $n = 1 \text{ cm}^{-3}$ for the ISM. The wind medium circumburst profile is governed by the mass-loss rate \dot{M} and wind velocity v_w . Therefore, we used $n = 10^{35} \dot{M}_{-5} / v_{w,3} \text{ cm}^{-3}$ for the wind medium (Ghirlanda et al. 2018). To determine the bulk Lorentz factor using the early bump, we have used the methodology described by Molinari et al. (2007; hereafter M2007).

3.2.3. Spectral Energy Distributions and Closure Relation

We created the SEDs using joint X-ray and optical data for both bursts to constrain the break frequencies of the broadband synchrotron model at two epochs for GRB 201015A and one epoch for GRB 201216C. We followed the methodology given in Hu et al. (2021), Caballero-García et al. (2022), and Gupta et al. (2022c) to create these SEDs. For GRB 201015A, the optical temporal index ($\alpha_o = -0.92_{-0.09}^{+0.08}$) follows a simple power-law decay post-optical bump and satisfies the relation $\alpha = (3p - 3)/4$ in the slow-cooling regime of the ISM, which indicates that the optical emission always remains in the $\nu_m < \nu_o < \nu_c$ spectral regime. The details of the epochs and temporal/spectral indices are given in Table B10 of the Appendix. For GRB 201015A, we performed follow-up observations with 3.6 m DOT in the BVRI filters. Our 3.6 m DOT optical observations covering the temporal window from 52 to 74 ks post burst are shown in Figure 7. We created an optical SED to calculate the optical spectral index β_{o2} and constrain the spectral regime at the epoch of DOT observations. The magnitudes are corrected for galactic extinction. In addition, we used negligible host extinction from Giarratana et al. (2022), and fitted a power-law function to determine the optical spectral index β_{o2} . We obtained a value of $\beta_{o2} = -1.13 \pm 0.30$. The calculated value of β_{o2} using DOT observations is shallower (~ 0.3) than the X-ray spectral index ($\beta_{x2} = -1.38_{-0.49}^{+0.47}$) at this epoch. The measured change in the spectral indices of the optical and X-ray data indicates that the

cooling frequency lies in between the optical and X-ray spectral regime, despite the large associated errors due to limited data points, and it is hard to discard other possibilities as β_{o2} and β_{x2} are consistent within 1σ . We noted that an ISM-type surrounding medium and $\nu_m < \nu_o < \nu_c < \nu_x$ spectral regime are also favored by the afterglow modeling of GRB 201015A by Giarratana et al. (2022) at this epoch, although they mainly use the preliminary optical magnitudes reported in various circulars. Using the calculated value of β_{o2} , we determined a power-law index of the electron distribution of $p = (2 \times \beta_{o2} + 1) = 3.26 \pm 0.60$ at this epoch.

For GRB 201015A, we create an optical to X-ray SED at two different epochs (as shown in Figure 7, upper panel). At the first epoch, the X-ray spectral index $\beta_{x1} = -1.07_{-0.30}^{+0.31}$ is shallower than (~ 0.3) the X-ray spectral index ($\beta_{x2} = -1.38_{-0.49}^{+0.47}$) at the second epoch. The evolution of the X-ray spectral index β_x also remains consistent within a 1σ error. We noted that ν_c is just below or within the XRT band spectral regime, also favored by the afterglow modeling (Giarratana et al. 2022) at this epoch. Considering no spectral break between the optical and X-ray emissions, we extrapolate the X-ray spectral index β_{x1} toward the optical band to estimate the intrinsic optical flux. By comparing the optical R -band flux with that obtained from the extrapolation, we determine an amount of extinction in the R band of $A_R = 2.2$ mag. At the second epoch, the cooling frequency ν_c has crossed the X-ray bands at ~ 52 ks.

For GRB 201216C, the late-time optical light curve seems to follow the normal decay with a power-law index of $\alpha_o = -1.05_{-0.10}^{+0.11}$. Additionally, the X-ray temporal index $\alpha_x = -2.21_{-0.10}^{+0.11}$ and the X-ray spectral index $\beta_x = -0.97_{-0.05}^{+0.05}$ remain almost constant throughout the emission. The X-ray/optical temporal/spectral indices satisfy the closure relation for a wind medium with emission $\nu_m < \nu_o < \nu_c < \nu_x$. A wind-type surrounding medium is also favored by the afterglow modeling of GRB 201216C by Rhodes et al. (2022).

For GRB 201216C, similarly, we created an optical to X-ray SED and extrapolated our X-ray spectral index (~ 2.5 hr) to the lower frequencies; see Figure 7, lower panel. The r -band magnitude corrected for Galactic extinction lies much below the extrapolated X-ray power-law slope. Considering no spectral break and a spectral break between X-ray and optical frequencies in the SED, we estimated the intrinsic optical flux by extrapolating the X-ray spectral index at r -band frequencies. By comparing the estimated optical flux to the observed VLT optical flux at 2.19 hr (Izzo et al. 2020), we determine a host extinction in the r band of $A_r \sim 8-5$ mag, supporting the dark nature of the burst, consistent with the result of Rhodes et al. (2022).

4. Discussion

4.1. Bulk Lorentz Factor and Characteristic Fireball Radius of VHE Detected GRBs

There are different ways to derive/put constraints on the bulk Lorentz factor of GRBs (Ghirlanda et al. 2018). In this section, we have derived the values of the bulk Lorentz factor for VHE detected GRBs using three different methods using the onset of the afterglow, Liang correlation, and the prompt $\Gamma_{\text{min}}-t_{\text{mvts}}$ relation.

Using the onset of the afterglow: We have used Equation (4) to calculate the bulk Lorentz factors for GRB 201015A, GRB 201216C, and the other four well-known VHE detected

Table 3
Summary of the Evaluation of the Lorentz Factors at various Characteristic Times and Radii for Seven VHE Detected GRBs

VHE Detected GRBs	M2007			L2010			G2015		
	t_p (s)	Γ_0	R_{dec} (cm)	T_{90} (s)	Γ_0	R_{em} (cm)	t_{mvts} (s)	$\Gamma_{0,\text{min}}$	R_c (cm)
160821B	0.5	69 ± 8	1.18×10^{14}	0.068	>88.74	2.78×10^{13}
180720B	<73	>576	$<2.19 \times 10^{17}$	49	506 ± 66	4.55×10^{17}	0.024	>457.20	1.82×10^{14}
190114C	<33.2	>341	$<4.10 \times 10^{16}$	25	407 ± 41	1.74×10^{17}	0.016	>472.86	1.53×10^{14}
190829A	63	76 ± 8	2.02×10^{16}	0.210	>47.74	2.67×10^{13}
201015A	184.64	204	8.16×10^{16}	9.78	143 ± 4	8.41×10^{15}	~ 0.1	>92.07	$\sim 4.81 \times 10^{13}$
201216C	179.9	310	1.23×10^{17}	29.9	513 ± 68	2.24×10^{17}	0.152	>286.99	3.60×10^{14}
221009A	<179	>440	$<4.50 \times 10^{17}$	327	>757	$<9.7 \times 10^{18}$	~ 0.001	>450.01	$\sim 1.1 \times 10^{13}$

GRBs, GRB 160821B (this GRB has no firm detection, but an evidence of a signal at VHE at the level of 3σ), GRB 180720B, GRB 190114C, and GRB 190829A. We noted that for the last four VHE GRBs, there are no early bumps/peaks observed in their optical afterglow light curves. For such cases, we assumed the earliest optical observations as upper limits for the peak time for the afterglow and constrained the lower limit on the bulk Lorentz factor for these bursts. The calculated values of Γ_0 using Equation (4) and the corresponding peak times are listed in the first column of Table 3, for both types of surrounding media. In addition, we also calculated the deceleration radius of the fireball at the peak time using the following equation taken from M2007:

$$R_{\text{dec}} = 2ct_p\Gamma_0^2/(1+z). \quad (5)$$

The calculated values of the deceleration radius are also listed in the first column of Table 3. Further, we also verified these parameters using various correlations between the bulk Lorentz factor and prompt emission properties, such as $\Gamma_0-E_{\gamma,\text{iso}}$ and $\Gamma_0-L_{\gamma,\text{iso}}$ and noted that the values are consistent for the subsample of VHE detected GRBs (see Figure A9).

Using Liang correlation: Liang et al. (2010; hereafter L2010) extensively searched for the onset of the afterglow in the X-ray and optical afterglow light curves using the published literature and Swift-XRT catalog. They found that 20 bursts in the optical and 12 bursts in the X-ray bands displayed the onset features in their corresponding afterglow light curves. In addition, L2010 also discovered tight correlations between the isotropic equivalent gamma-ray energy $E_{\gamma,\text{iso}}$ and the initial bulk Lorentz factor of the fireball. The correlation can be given as: $\Gamma_0 \sim 182(E_{\gamma,\text{iso}}/10^{52} \text{ erg})^{(0.25 \pm 0.03)}$.

For the seven known VHE detected GRBs, we derive the bulk Lorentz factor using the $\Gamma_0-E_{\gamma,\text{iso}}$ correlation, and the calculated values along with T_{90} are listed in the second column of Table 3. We also calculated the fireball radius at the end of the prompt emission using the following relation: $R_{\text{em}} = 2ct\Gamma_0^2/(1+z)$, using $t \sim T_{90}$ in the equation. The calculated values of the fireball radius given are also listed in the second column of Table 3.

Additionally, L2010 also studied the correlations between the characteristic bump/onset parameters, such as the peak time, FWHM, isotropic gamma-ray energy and they found that most of these parameters are strongly correlated with each other. We also compare the properties of the observed bump in the early optical light curves of GRB 201015A and GRB 201216C with the known correlations. We noted that most of the characteristic parameters of the observed bump in the early optical light curves of GRB 201015A and

GRB 201216C are consistent with the correlations studied by L2010, confirming the nature of the bumps due to the onset of forward shocks in the external ambient medium. However, GRB 201216C does not follow the correlation between $E_{\gamma,\text{iso}}$ and the optical peak luminosity ($L_{p,\text{opt}}$), supporting the dark behavior of GRB 201216C (Rhodes et al. 2022). The correlations between the different parameters of the optical bumps of GRB 201015A and GRB 201216C, along with data taken from L2010, are shown in Figure A10 of the Appendix.

Using the prompt $\Gamma_{\text{min}}-t_{\text{mvts}}$ relation: In addition to the above methods, we also used the prompt $\Gamma_{\text{min}}-t_{\text{mvts}}$ (minimum variability timescales) relation to calculate the lower bound on the bulk Lorentz factor (Γ_{min}) and to calculate the emission radius during the prompt emission phase. We used the following relations between $\Gamma_{\text{min}}-t_{\text{mvts}}$ and R_c-t_{mvts} derived by Golkhou et al. (2015; hereafter G2015):

$$\Gamma_{\text{min}} \geq 100 \left(\frac{L_{\gamma,\text{iso}}}{10^{51} \text{ erg s}^{-1}} \frac{1+z}{t_{\text{mvts}}/0.1 \text{ s}} \right)^{1/5} \quad (6)$$

$$R_c \sim 7.3 \times 10^{13} \left(\frac{L_{\gamma,\text{iso}}}{10^{51} \text{ erg s}^{-1}} \right)^{2/5} \left(\frac{t_{\text{mvts}}/0.1 \text{ s}}{1+z} \right)^{3/5} \text{ cm}. \quad (7)$$

We calculated the minimum variability timescales for the VHE detected GRBs using the Bayesian block method on the prompt emission light curve in the energy ranges of 8–900 keV for Fermi-GBM and 15–350 keV for Swift-BAT. The Bayesian blocks utilize the statistically significant changes to bin the prompt emission light curves of these bursts. We determine the minimum bin size, and the minimal variability timescales are equal to half of the width of the smallest bin of Bayesian blocks (Vianello et al. 2018). The calculated values of t_{mvts} , Γ_{min} , and R_c are listed in the third column of Table 3. We noted that the emission radius lies in the range of 2×10^{13} – 4×10^{14} cm for the seven known VHE detected GRBs, consistent with the results of G2015. The calculated emission radius for these VHE detected GRBs is much larger than the typical emission radius of the photosphere, suggesting that the emission took place in an optically thin region away from the central engine (Burgess et al. 2020; Caballero-García et al. 2022).

4.2. Lorentz Factor Evolution and Possible Jet Composition

The evolution of the bulk Lorentz factor can provide insight into the jet composition, the prompt emission location, and the radiation physics of GRBs. The jets of GRBs can be matter dominated (originated due to photosphere) or Poynting flux dominated (originated due magnetic reconnection). However, a third hybrid jet composition (quasi-thermal component together with a nonthermal component) formed in the internal shocks, is possible. In such a hybrid case, it is expected that the Lorentz

factor remains almost constant during the prompt emission phase and decreases during the onset of the afterglow (Lin et al. 2019). On the other hand, in the case of a Poynting-flux-dominated jet (a part of the magnetic field energy dissipates to accelerate the GRB jet), the Lorentz factor measured during the onset of the afterglow is expected to be larger than that measured during the prompt phase (Zhang & Zhang 2014).

In Section 4.1, we have calculated the bulk Lorentz factor of the fireball for GRB 201015A and GRB 201216C at different epochs to examine the evolution of the Lorentz factor and constrain the possible jet composition. Initially, we calculated the bulk Lorentz factor values during the prompt emission phase using two different methods: the first one using the relation between the lower limit of the bulk Lorentz factor $\Gamma_{0,\min}$ and the minimum variability timescale t_{mvtS} (G2015). In the second method, we have used the tight correlation between Γ_0 and the total isotropic gamma-ray energy released during the prompt emission to calculate the bulk Lorentz factor (L2010). Finally, we calculated the bulk Lorentz factor values (for the different types of ambient medium) during the onset of forward-shock emission using the observed early peak in the optical afterglow light curves (Sari & Piran 1999; Molinari et al. 2007; Ghirlanda et al. 2018).

In the case of GRB 201015A, the measured values of Γ_0 at different epochs are: >92.07 using G2015, 143 using L2010, and 204 for an ISM-like medium using the onset of forward-shock emission. The lower limit on the measured value of Γ_0 (using G2015) is consistent with that measured using the tight correlation between Γ_0 and $E_{\gamma,\text{iso}}$. For GRB 201015A, the closure relations support a homogeneous medium (see Section 3.2.3), also consistent with Giarratana et al. (2022). The value of the bulk Lorentz factor during the onset of the afterglow increases for an ISM-like ambient medium, supporting a Poynting-flux-dominated jet composition for GRB 201015A, although there is not a very large difference between the bulk Lorentz factor values at different epochs. In the case of GRB 201216C, the measured values of Γ_0 at different epochs are: >286 using G2015, 513 using L2010, and 310 for a wind-like medium using the onset of forward-shock emission. For this GRB also, the lower limit on Γ_0 (using G2015) is lower than that measured using tight correlation between Γ_0 and $E_{\gamma,\text{iso}}$. For GRB 201216C, the closure relations support a wind-like medium (see Section 3.2.3), also consistent with Rhodes et al. (2022). The value of the bulk Lorentz factor during the onset of the afterglow decreases for a wind-like ambient medium, supporting a matter-dominated jet composition for GRB 201216C.

4.3. Progenitors of GRB 201015A and GRB 201216C: Collapsar Origin?

The recent discoveries of short GRBs (GRB 200826A, GRB 211227A) from the collapse of massive stars (Ahumada et al. 2021; Lü et al. 2022) and a long GRB (GRB 211211A) from binary mergers (Rastinejad et al. 2022) challenge our understanding about the progenitor systems of GRBs. In this section, we examine the possible progenitors of GRB 201015A and GRB 201216C. There are two possible models (collapsar and binary merger) for the progenitors of GRBs. According to the collapsar model, the central engine (black hole or magnetar) forms after the death of a massive stellar object, which emits a jet that successfully penetrates the preexisting envelope around the progenitor star. If the jet does not have sufficient energy to

break out, it deposits all of its energy into the surrounding envelope to form a mildly relativistic cocoon around it. This process is known as shock breakout, and it gives emission in gamma rays, with a luminosity 2–3 orders less than that of typical long GRBs (Bromberg et al. 2011). Such a subclass of GRBs with low isotropic gamma-ray luminosity (order of 10^{46} – 10^{49} erg s^{-1}) emitted during the prompt emission phase is assumed to have a different origin than normal long GRBs. In the VHE detected GRB sample, GRB 190829A is a peculiar low-luminosity GRB with no shock-breakout origin (Chand et al. 2020). In addition, GRB 201015A also belongs to the low-luminosity family of GRBs with a supernova bump in the late optical light curve, which motivate us to test whether it has a collapsar or shock-breakout origin.

In the case of a collapsar origin, it is expected that the observed duration (T_{90}) of the burst should be greater than the jet breakout time (T_{break}) from the surrounding envelope. Bromberg et al. (2011) suggested that if the ratio $T_{90}/T_{\text{break}} < 1$ and the jet fails to cross the envelope, the burst is expected to originate from shock breakout. On the other hand, if $T_{90}/T_{\text{break}} > 1$ and the jet successfully crosses the envelope, the burst is expected to originate from a collapsar. We calculated the jet breakout time for GRB 201015A following the equation given by Bromberg et al. (2011): $T_{\text{break}}(\text{s}) \sim 15 \epsilon_{\gamma}^{1/3} L_{\gamma,\text{iso},50} \theta_{10}^{2/3} R_{11}^2 M_{15\odot}^{1/3}$.

The jet breakout time depends on the isotropic equivalent luminosity, the observed opening angle, the progenitor mass, and the radiation efficiency. To calculate T_{break} for GRB 201015A, we assume the typical values of $M = 15M_{\odot}$, $\theta = 10^\circ$, and $\epsilon_{\gamma} = 0.2$ (Bromberg et al. 2011). We obtained a ratio T_{90}/T_{break} of 1.75 for GRB 201015A, which supports the collapsar origin of the burst. We also calculated the T_{90}/T_{break} ratio for GRB 201216C considering $\theta = 1^\circ$ and 9° with progenitor masses of $12M_{\odot}$ and $25M_{\odot}$ (Rhodes et al. 2022) and found that T_{90}/T_{break} lies in the range of 30–163, which confirms the collapsar origin of GRB 201216C.

4.4. Comparison of GRB 201015A and GRB 201216C with other VHE Detected GRBs

In the seven cases of VHE GRBs, VHE photons were detected during the afterglow phase, although VHE photons may also enrich the prompt emission of GRBs. In the present section, we compared the afterglow results obtained for GRB 201015A and GRB 201216C (see Section 3) with a sample of well-known VHE detected GRBs (Fraija et al. 2019b; MAGIC Collaboration et al. 2019a, 2019b; Nava 2021; Noda & Parsons 2022). In addition to afterglow comparison, we also collected the prompt emission properties of VHE detected GRBs, as listed in Table 1.

4.4.1. Comparison of the X-Ray and Optical Afterglow Light Curves of VHE Detected GRBs

In the present section, we compare the X-ray and the optical (see Figure A7 of the Appendix) afterglow luminosity light curves of GRB 201015A and GRB 201216C with other well-studied VHE detected GRBs (GRB 160821B, GRB 180720B, GRB 190114C, GRB 190829A, and GRB 221009A). In addition, we also include the X-ray (if available) and optical (if available) light curves of a nearly complete sample of nearby and supernovae-connected GRBs (GRB 050525A/SN 2005nc ($z = 0.606$), GRB 081007A/SN 2008hw ($z = 0.530$), GRB 091127A/SN 2009nz ($z = 0.490$), GRB 101219B/SN 2010ma

($z = 0.552$), GRB 111209A/SN 2011kl ($z = 0.677$), GRB 130702A/SN 2013dx ($z = 0.145$), GRB 130831A/SN 2013fu ($z = 0.479$), GRB 060218/SN 2006aj ($z = 0.033$), GRB 120422A/SN 2012bz ($z = 0.282$), GRB 130427A/SN ($z = 0.340$), GRB 190114C/SN ($z = 0.425$), GRB 190829A/SN 2019oyw ($z = 0.078$), and GRB 200826A/SN ($z = 0.748$)) for comparison as most of VHE detected bursts are nearby and connected with supernovae. The comparison of the X-ray afterglow light curves indicates that VHE detected GRB 180720B and GRB 201216C have extremely bright X-ray emission (just below the brightest X-ray emission observed from GRB 130427A at early epochs). GRB 221009A and GRB 190114C also have very bright X-ray emissions but less than those of GRB 180720B and GRB 201216C at early epochs. On the other hand, GRB 160821B, GRB 190829A, and GRB 201015A have faint X-ray emission. The X-ray afterglow of GRB 201015A has a nearly comparable brightness with GRB 190829A. GRB 160821B, being a short burst, has the faintest X-ray light curve (after the steep-decay phase) with respect to present VHE sample.

For the optical afterglow light-curve comparison, we collected the R -band light curves of VHE detected GRBs (other than GRB 221009A) from the literature (Fraija et al. 2019b; MAGIC Collaboration et al. 2019a; Jordana-Mitjans et al. 2020; Gupta et al. 2021b; Misra et al. 2021). For GRB 221009A, we collected the optical data from the GCN circulars.²¹ For a nearly complete sample of nearby and supernovae-connected GRBs, we obtained the optical data from Kumar et al. (2022a) and references therein. We noted that GRB 180720B has the highest optical luminosity at early epochs in comparison to the present sample (similar to the X-ray light curve), and the light curve displays a smooth power-law decay across the emission period (Fraija et al. 2019b). At later phases (~ 0.2 day post burst), GRB 221009A seems to have the highest optical luminosity in comparison to the present sample. In the case of GRB 201216C, despite the very bright X-ray emission, the optical light curve is one of the faintest among those of the present sample, typical to those observed in the case of dark GRBs. Further, we noted that GRB 201015A and GRB 201216C have comparable optical luminosity light curves. GRB 190114C (Gupta et al. 2021b), GRB 190829A (Hu et al. 2021), and GRB 201015A (Giarratana et al. 2022) exhibited late-time bumps in their optical light curves associated with their underlying supernovae explosions. In addition, we noted that GRB 201015A and GRB 201216C are the only the bursts with very early smooth bumps (the onset of the forward shock) in their optical light curves among the present sample.

4.4.2. Possible Origin of VHE Emission from High- and Low-luminosity Bursts

The broadband afterglow observations of the VHE detected GRBs could not be explained by the typical external-shock synchrotron model (MAGIC Collaboration et al. 2019b; HESS Collaboration et al. 2021). The multiwavelength modeling of the observed double-bump SEDs of VHE detected GRBs demands an additional SSC/inverse Compton component. VHE detected GRBs are expected to be luminous and nearby such as GRB 180720B, GRB 190114C, and GRB 221009A. However, some of the recent detection of VHE emission from

low/intermediate-luminosity bursts (such as GRB 190829A and GRB 201015A), pose a new question about their possible progenitors and viewing geometry. The high-luminosity GRBs are typically observed on-axis with narrow viewing; on the other hand, low-luminosity bursts are typically observed off-axis with wide viewing angles. Recently, some authors (Rhodes et al. 2022; Sato et al. 2022) used two different jet components (narrow and wide) to explain the origin of the observed properties of high- and low-luminosity VHE detected GRBs. According to this model, the early broadband emission of high-luminosity GRBs are explained using a narrow jet component with typical opening angle $\theta < 0^\circ.86$. On the other hand, low-luminosity GRBs are explained using a wide jet component with typical opening angle $\theta > 6^\circ$ (Sato et al. 2022). Sato et al. (2022) performed broadband modeling of the nearby and low-luminosity GRB 190829A using a two-component jet model and noted that the prompt and afterglow emissions could not be described by a narrow jet component. The observed low/intermediate-luminosity nature of GRB 190829A is explained by assuming that the viewing angle is greater than the opening angle of its narrow jet component (off-axis observations). GRB 201015A is also a nearby intermediate-luminosity GRB and might have a very similar viewing geometry to GRB 190829A (viewing angle greater than the narrow jet opening angle). In the cases of GRB 180720B and GRB 190114C, the observed high-luminosity nature of these GRBs is explained by emission within a narrow jet component (on-axis observations). The same applies to GRB 201216C, given its observed high luminosity.

The observed typical sub-TeV bumps are explained either using SSC or external inverse Compton scattering (Abdalla et al. 2019; MAGIC Collaboration et al. 2019b). According to the two-component model, during the early phase, both components (narrow and wide) of the jet have almost equal velocities. This negligible difference in the velocities helps to discard the possibility of the contribution from the external inverse Compton during the early phase (Sato et al. 2022). Therefore, the SSC emission mechanism is expected to explain the early VHE emission in, e.g., GRB 190114C and GRB 190829A (MAGIC Collaboration et al. 2019b; HESS Collaboration et al. 2021). In the case of GRB 180720B, VHE photons were observed several hours after the detection. Therefore, considering the two jets moving at different velocities, inverse Compton significantly contributed to the observed VHE emission (Abdalla et al. 2019). In the case of GRB 201216C, considering the synchrotron process as a possible radiation mechanism at $t \sim 3 \times 10^3 - 10^4$ s post burst at X-ray frequencies, we extrapolated the X-ray spectral index β_x toward GeV–TeV energies (for the spectral regime $\nu_c < \nu_x$), and estimated an expected flux density of $F_\nu \sim 2.3 \times 10^{-11}$ Jy and $F_\nu \sim 3 \times 10^{-13}$ Jy at 1 GeV and 0.1 TeV, respectively. Fermi-LAT could not detect the GeV emission from GRB 201216C during the interval $T_0 + 3500$ s to $T_0 + 5500$ s post burst. This is in agreement with the fact that the expected flux density at 1 GeV at $t \sim 3 \times 10^3 - 10^4$ s post burst is below the sensitivity of the Fermi-LAT instrument. Furthermore, from the observed peak in the early optical light curve of GRB 201216C, we calculated the initial Lorentz factor of the burst to be $\Gamma \sim 300$. With this Lorentz factor and $z = 1.1$, photons of maximum energy, ≤ 15 GeV, are allowed by synchrotron process (Fraija et al. 2019b).

²¹ <https://gcn.gsfc.nasa.gov/other/221009A.gcn3>

Similarly, for GRB 201015A an expected flux density of $F_\nu \sim 3.8 \times 10^{-13}$ Jy and $F_\nu \sim 2.8 \times 10^{-15}$ Jy at 1 GeV and 0.1 TeV, respectively, is obtained at 3–5 ks. A bulk Lorentz factor of ~ 200 is obtained from the observed peak in the optical light curve. With this Lorentz factor and $z = 0.426$, we estimated the maximum energy of synchrotron photons to be ≤ 14 GeV (Fraija et al. 2019b).

Therefore, the observed early VHE emission could not be explained using the synchrotron emission model. The previous discussion suggests that the early detection of VHE photons from GRB 201015A and GRB 201216C required that the ultrarelativistic outflow boosts the energy of low-energy synchrotron photons to VHE via the SSC process.

5. Summary and Conclusion

In this work, we presented a detailed analysis of the prompt and afterglow emission of two VHE detected GRBs, GRB 201015A and GRB 201216C, and their comparison with a subset of similar bursts. In spite of showing prompt-emission characteristics of other typical LGRBs, GRB 201015A is a low/intermediate-luminosity GRB, whereas GRB 201216C is one of the high-luminosity ones. Detailed time-resolved spectral analysis of Fermi observations of GRB 201216C suggests that the low-energy spectral index (α_{pt}) remained within the expected values of the synchrotron slow- and fast-cooling limits, supporting the synchrotron emission as a possible emission mechanism. Searches for an additional thermal component indicate that some of the Bayesian bins have a quasi-thermal component centered around the beginning or near the peaks of the light curve. Further, we studied the evolution of the spectral parameters and found a rare feature where E_p and α_{pt} both exhibit a flux-tracking behavior (double tracking) throughout the duration of GRB 201216C as published recently (Gupta et al. 2021a), proposing the observed relation between E_p and flux in terms of fireball cooling and expansion. In such a scenario, during the fireball expansion, the magnetic field reduces resulting in a lower intensity and E_p . However, increased central-engine activity during the bursting phase might increase the magnetic field, resulting in a higher E_p and/or intensity. If such a scenario is true, the magnetic field should be strongly correlated with E_p (Gao et al. 2021). Interestingly, we found a strong correlation between E_p (derived using the empirical Band function) and the magnetic field B (derived using the physical Synchrotron model), supporting our results discussed above. On the other hand, the strong correlation observed between α_{pt} and the flux can be explained in terms of subphotospheric heating in a flow of varying entropy (Ryde et al. 2019).

Our earliest optical observations of the afterglow of GRB 201015A using FRAM-ORM and BOOTES and GRB 201216C using the FRAM-ORM robotic telescope display smooth bumps, consistent with the onset of the afterglows in the framework of the external forward-shock model (Sari & Piran 1999). Using the observed optical peak, we determined the initial bulk Lorentz factors of GRB 201015A and GRB 201216C: $\Gamma_0 = 204$ for the ISM-like and $\Gamma_0 = 310$ for the wind-like ambient media, respectively. Further, we studied the evolution of the Lorentz factors and constrained the

possible jet compositions for both bursts. The evolution of the Lorentz factors suggests a Poynting-flux-dominated jet for GRB 201015A, whereas for GRB 201216C an internal-shock-dominated jet consistent with time-resolved spectral analysis is preferred. Furthermore, we investigated the possible progenitors of GRB 201015A and GRB 201216C by constraining the time taken by the jets to break through the surrounding envelopes (T_{break}) using the relation given by Bromberg et al. (2011) and taking the ratios of the observed T_{90} to T_{break} . We find that for both bursts, this ratio is greater than 1, suggesting collapsars as the possible progenitor of GRB 201015A and GRB 201216C. Further, late-time optical follow-up observations of GRB 201015A reveal an associated supernova (Giarratana et al. 2022), additional evidence confirming the collapsar origin.

Finally, we compared the properties of GRB 201015A and GRB 201216C with other similar VHE detected GRBs. Our findings suggest that VHE emission is common both in high- and low-luminosity GRBs. Our study also suggests that the SSC process is needed to explain the VHE emission of these bursts. Early follow-up observations of similar sources using robotic telescopes are very crucial not only to constrain the Lorentz factors/their evolution but also to decipher other less explored aspects of underlying physics like the radiation mechanisms and jet composition.

The authors are thankful to the anonymous referee for his/her positive and valuable comments. R.G. and S.B.P. acknowledge the financial support of ISRO under AstroSat archival Data utilization program (DS_2B-13013(2)/1/2021-Sec.2). A.A. acknowledges funds and assistance provided by the Council of Scientific & Industrial Research (CSIR), India with file No. 09/948(0003)/2020-EMR-I. A.J.C.T. acknowledges support from the Spanish Ministry project PID2020-118491GB-I00 and Junta de Andalucía grant P20_010168. Y.D.H. acknowledges support under the additional funding from the RYC2019-026465-I. M.C.G. acknowledges support from the Ramón y Cajal Fellowship RYC2019-026465-I (funded by the MCIN/AEI/10.13039/501100011033 and the European Social Funding). This research has used data obtained through the HEASARC Online Service, provided by the NASA-GSFC, in support of the NASA High Energy Astrophysics Programs. S.B.P. thankfully acknowledges inclusion of the photometric calibration data of GRB 201015A taken with the $4K \times 4K$ CCD Imager acquired as a part of the present analysis and extends sincere thanks to the observing and support staff of the 3.6 m DOT for maintaining and running the observational facilities at Devasthal Nainital.

Facilities: FRAM-ORM, BOOTES, 3.6 m DOT (IMAGER).

Software: DAOPHOT-II (Stetson 1987), IRAF (Tody 1986, 1993), 3ML (Vianello et al. 2015), XSPEC (Arnaud 1996), HOTPANTS (Becker 2015), Astropy (Astropy Collaboration et al. 2013), Matplotlib (Hunter 2007).

Appendix A Additional Figures

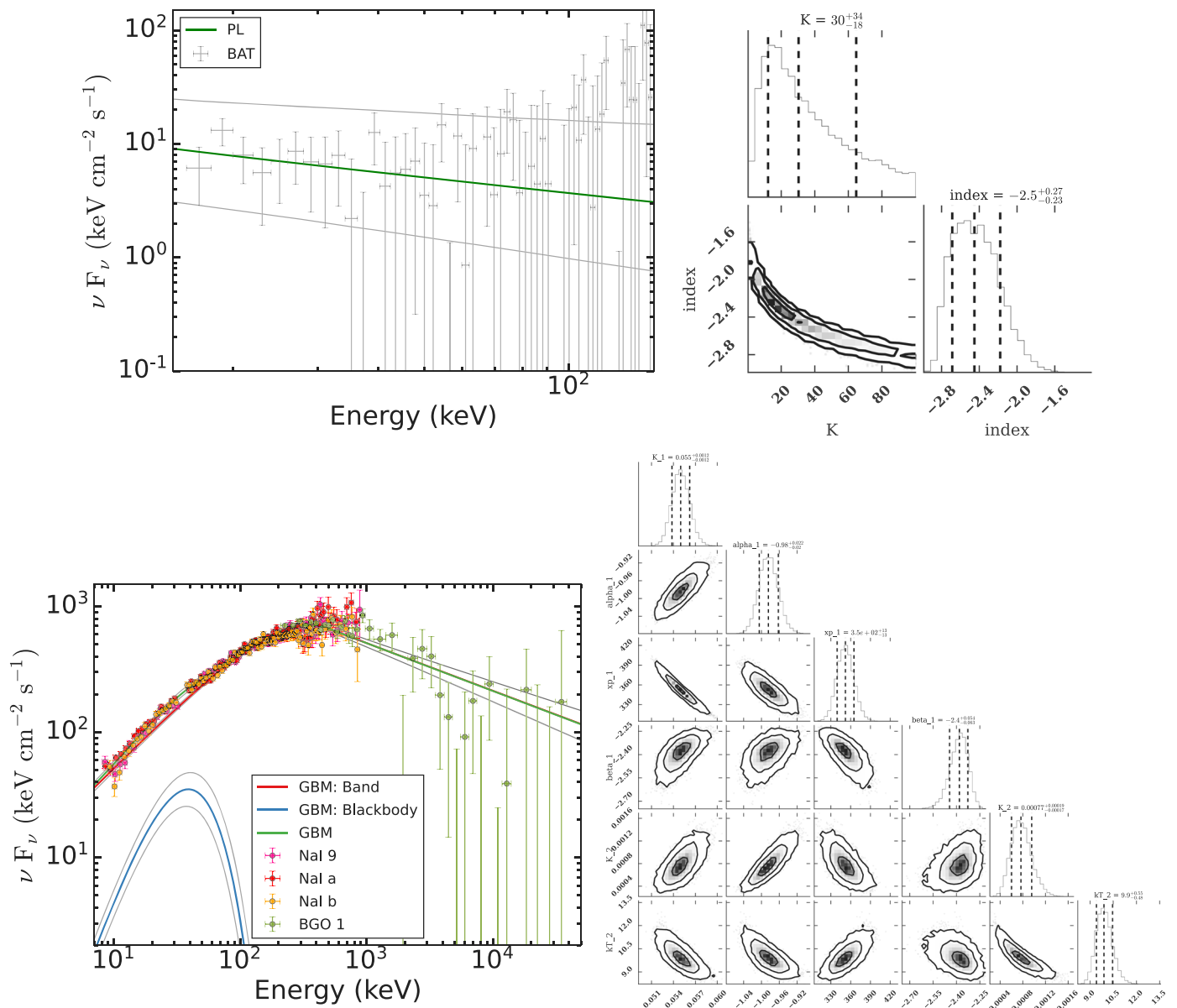


Figure A1. Best-fit time-averaged energy spectrum using the power-law (for GRB 201015A) and Band + Blackbody (for GRB 201216C) models. The green solid lines (for GRB 201015A and GRB 201216C) show the best-fit energy spectra of the models. The corresponding white shaded regions show the 95% confidence interval. The right plots show the corresponding corner plots for the best-fit models.

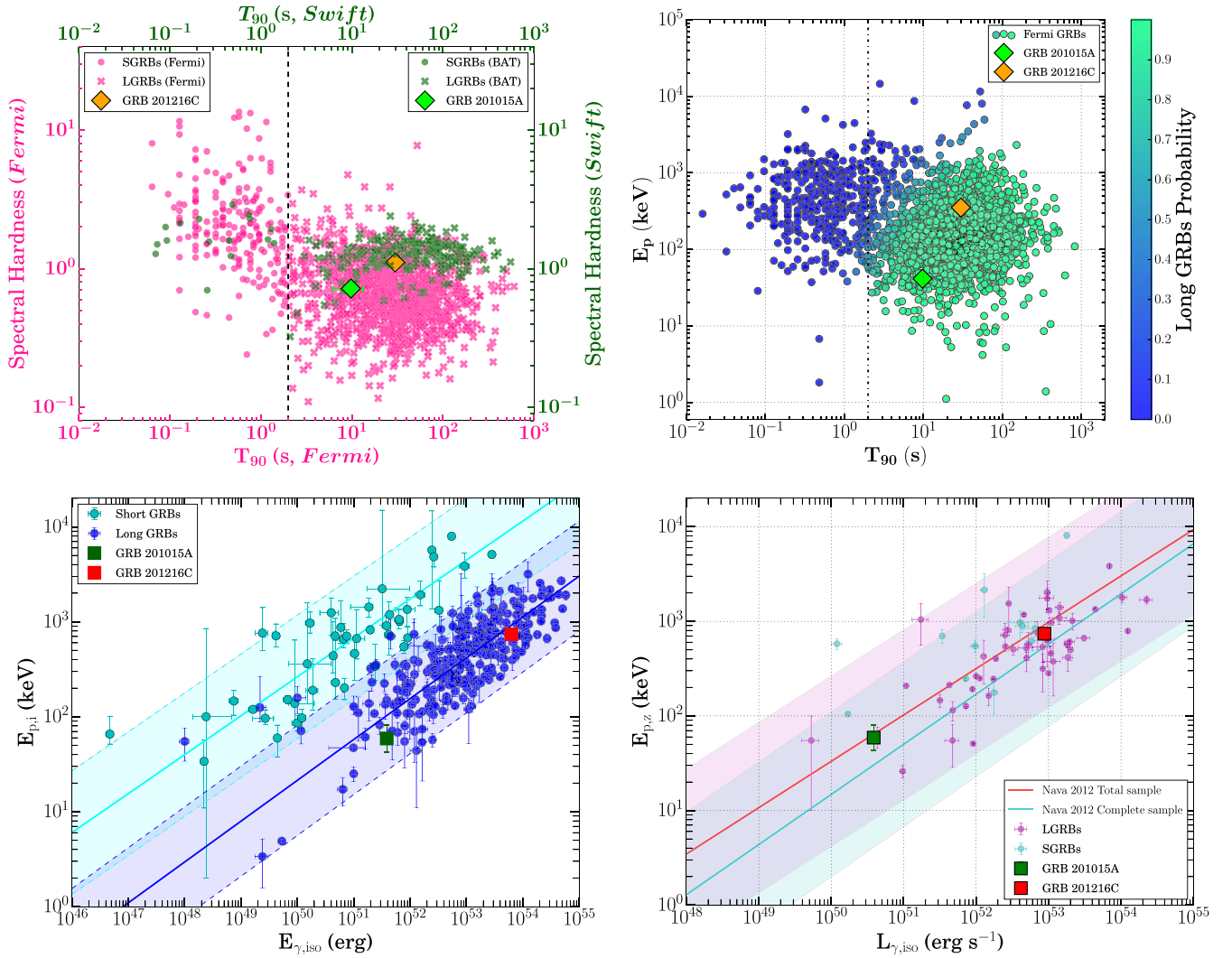


Figure A2. Top left panel: Hardness ratio and T_{90} distribution plane for the GRBs detected by Swift-BAT (green) and Fermi-GBM (deep pink). Top right panel: E_p - T_{90} distribution plane for the GRBs detected by Fermi-GBM (Goldstein et al. 2017). The right-side color bar denotes the probability of the GRB being a long burst. The locations of GRB 201015A and GRB 201216C are shown with lime and orange diamonds, respectively. The black dashed vertical line denotes the boundary between long and short bursts. Bottom left panel: Amati correlation of prompt emission. GRB 201015A and GRB 201216C are represented by the green and red squares, respectively, while the cyan and blue dots represent the short and long GRBs collected from Minaev & Pozanenko (2020). Bottom right panel: Yonetoku correlation of prompt emission. GRB 201015A and GRB 201216C are represented by the green and red squares, respectively, along with the GRB sample reported in Nava et al. (2012). The best-fit is shown by several solid colored lines, and the shaded region represents the 3σ scatter of the correlation.

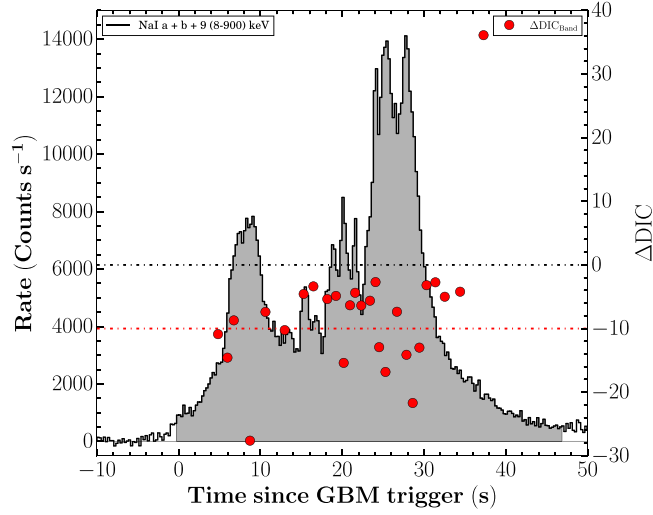


Figure A3. Evolution of Δ DIC within the burst interval for the Band and Band + Blackbody models for GRB 201216C. The black dotted line is at Δ DIC = 0; the data points below indicate an improvement in the fit after adding the Blackbody function. The red dotted line is at Δ DIC = -10; the data points below indicate a significant amount of thermal components in the corresponding spectrum.

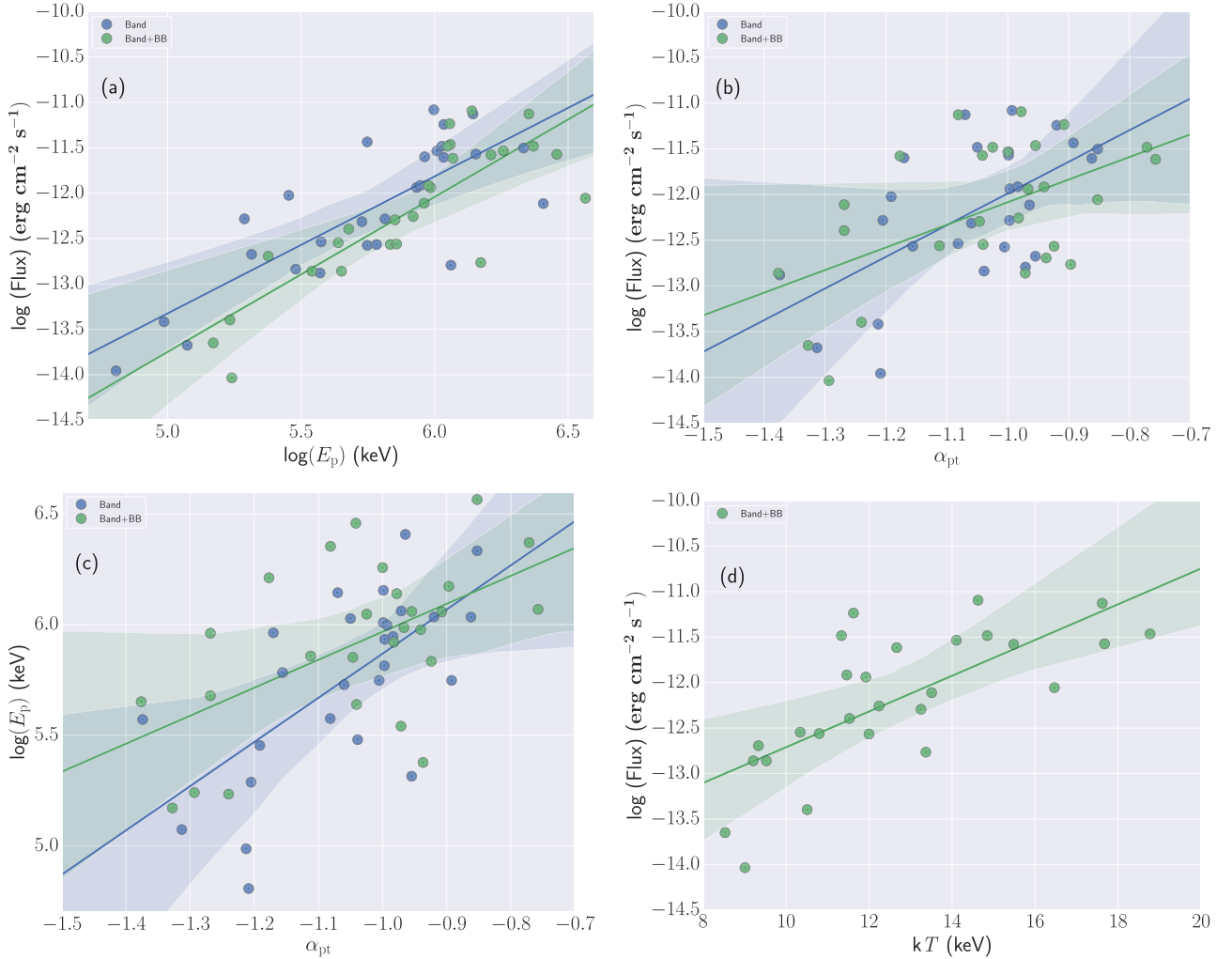


Figure A4. Correlations between the spectral parameters obtained from the fitting of the Band and Band + Blackbody models to the GBM data for GRB 201216C. (a) Correlation between the $\log(\text{flux})-\log(E_p)$ obtained from the Band (blue) and Band + Blackbody (green) models. Similarly, (b) and (c) represent the correlation between $\log(\text{flux})-\alpha_{pt}$ and $\log(E_p)-\alpha_{pt}$. (d) represents the correlation between $\log(\text{flux})-kT$ obtained from the Band + Blackbody model. The solid lines represent the best fit, and the shaded region shows the 2σ confidence interval of the correlation.

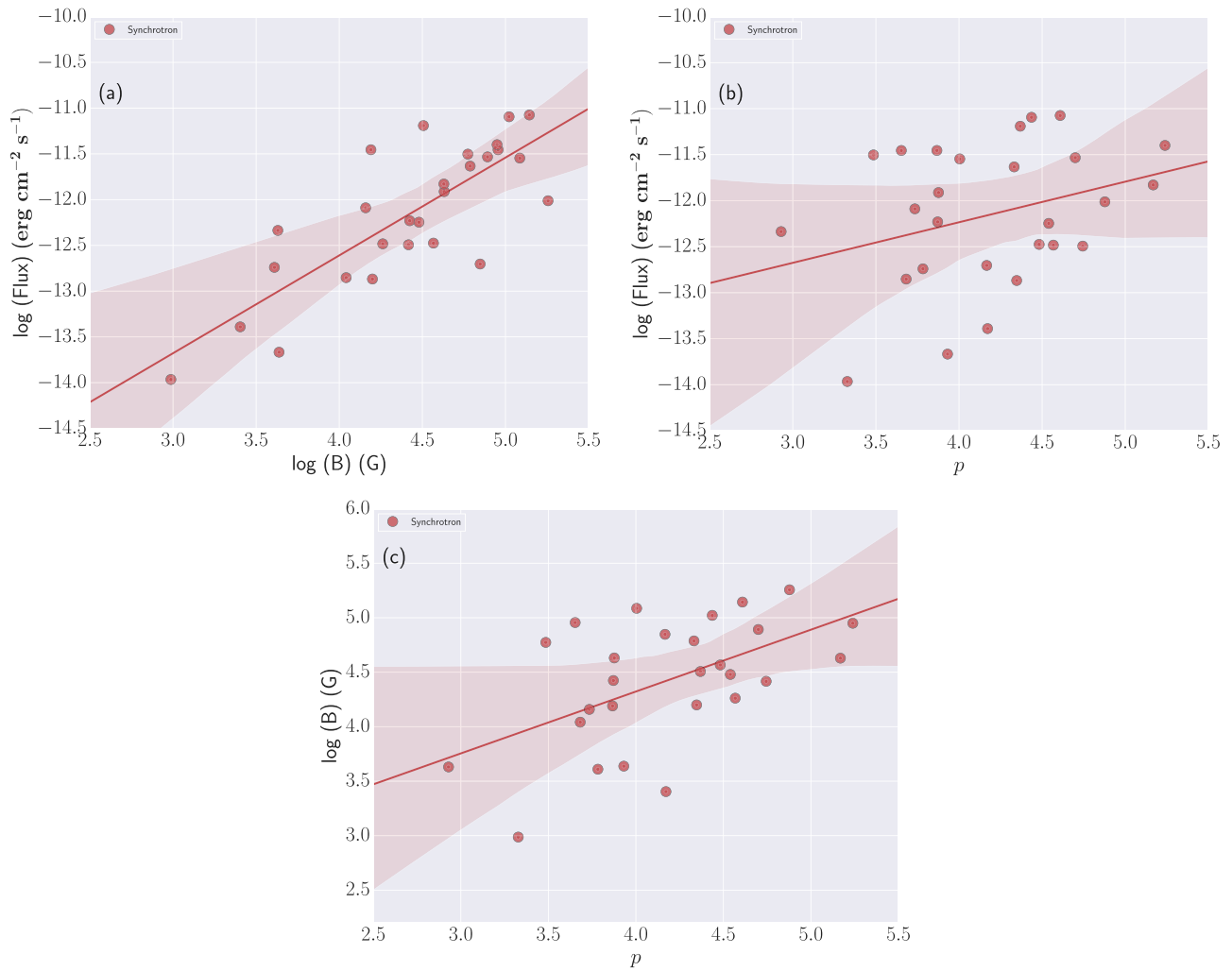


Figure A5. Correlations between the spectral parameters obtained from fitting the physical Synchrotron model to the GBM data for GRB 201216C. (a) Logarithm of the magnetic field strength B vs. $\log(\text{flux})$, (b) electron energy index p vs. $\log(\text{flux})$, and (c) $\log(B)$ vs. p . The solid red lines represent the best fit, and the shaded region shows the 2σ confidence interval of the correlation.

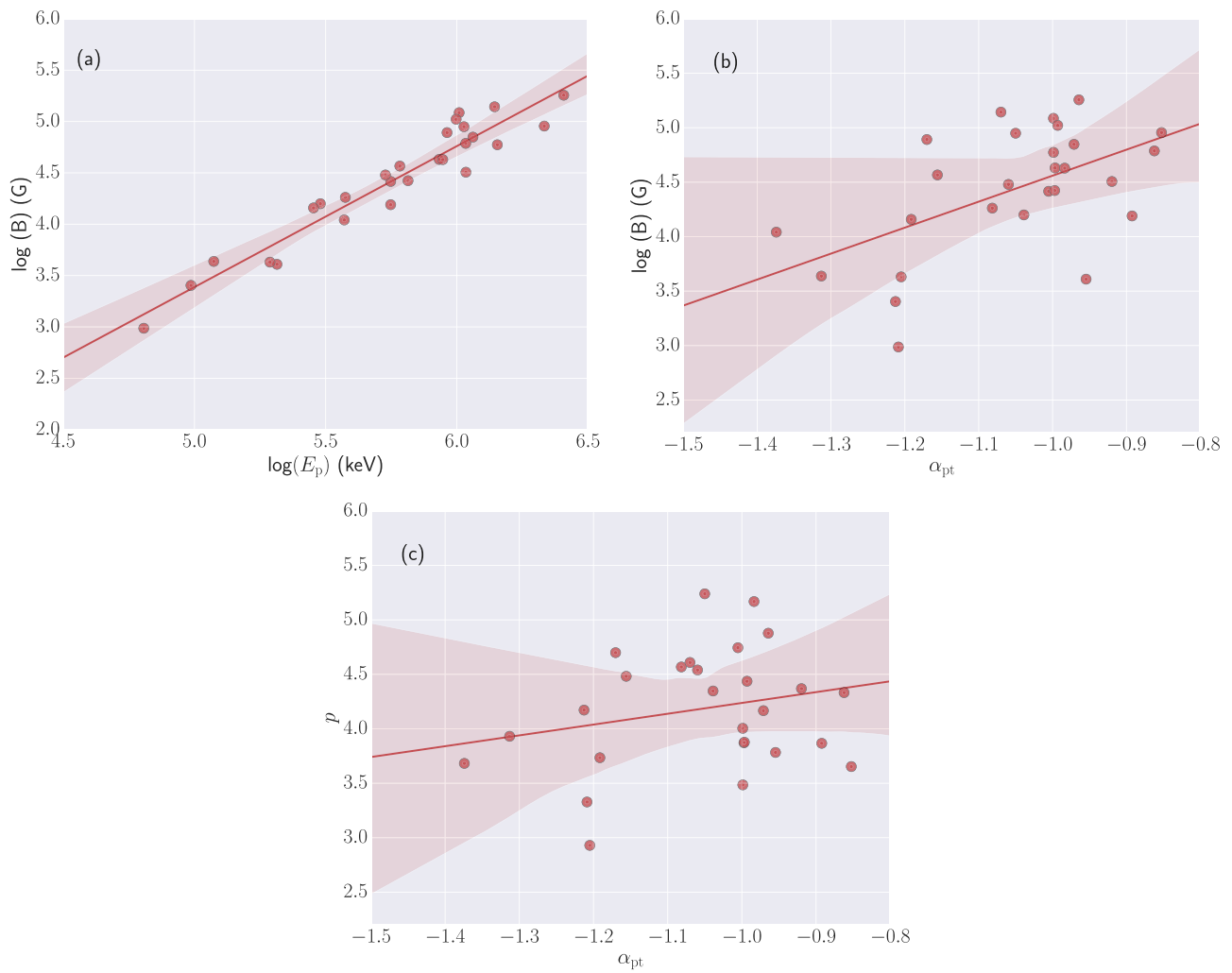


Figure A6. Correlations between the spectral parameters obtained from the `Synchrotron` and `Band` models to the GBM data for GRB 201216C. (a) Logarithm of the magnetic field strength B vs. $\log(E_p)$, (b) logarithm of the magnetic field strength B vs. $\log(\alpha_{pt})$, (c) electron energy index p vs. α_{pt} . The solid red lines represent the best fit, and the shaded region shows the 2σ confidence interval of the correlation.

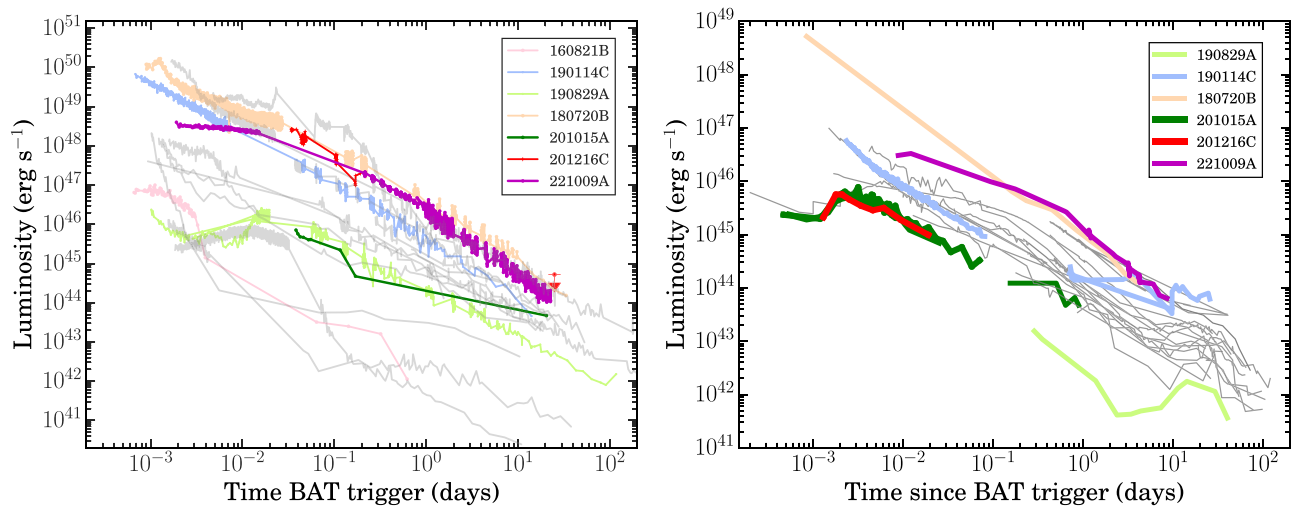


Figure A7. Comparison of the afterglow light curves of VHE detected GRBs. Left panel: X-ray (@ 0.3–10 keV) light curves of VHE detected GRBs represented by various colors, as shown in the legends. The light curves shown in the background with the gray color are a sample of nearby supernova-connected GRBs taken from Kumar et al. (2022a). Right panel: comparison among the optical light curves of VHE detected GRBs and a sample of nearby supernova-connected GRBs in the R band.

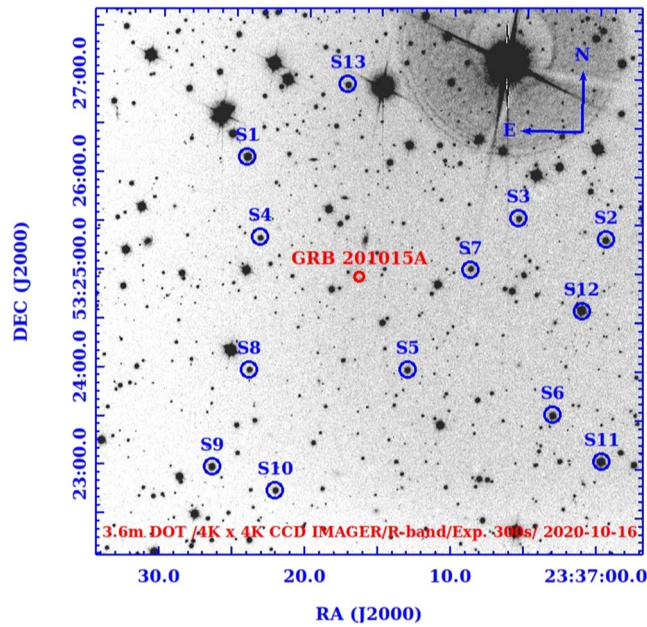


Figure A8. The finding chart of GRB 201015A observed in the R band utilizing the 4 K × 4 K CCD Imager mounted on the 3.6 m DOT (Kumar et al. 2022b). The arrows in the image denote the directions (north and east). The stars marked with S1 to S13 are used to calibrate the magnitude in the standard system. The image has an FoV of 6'5 × 6'5.

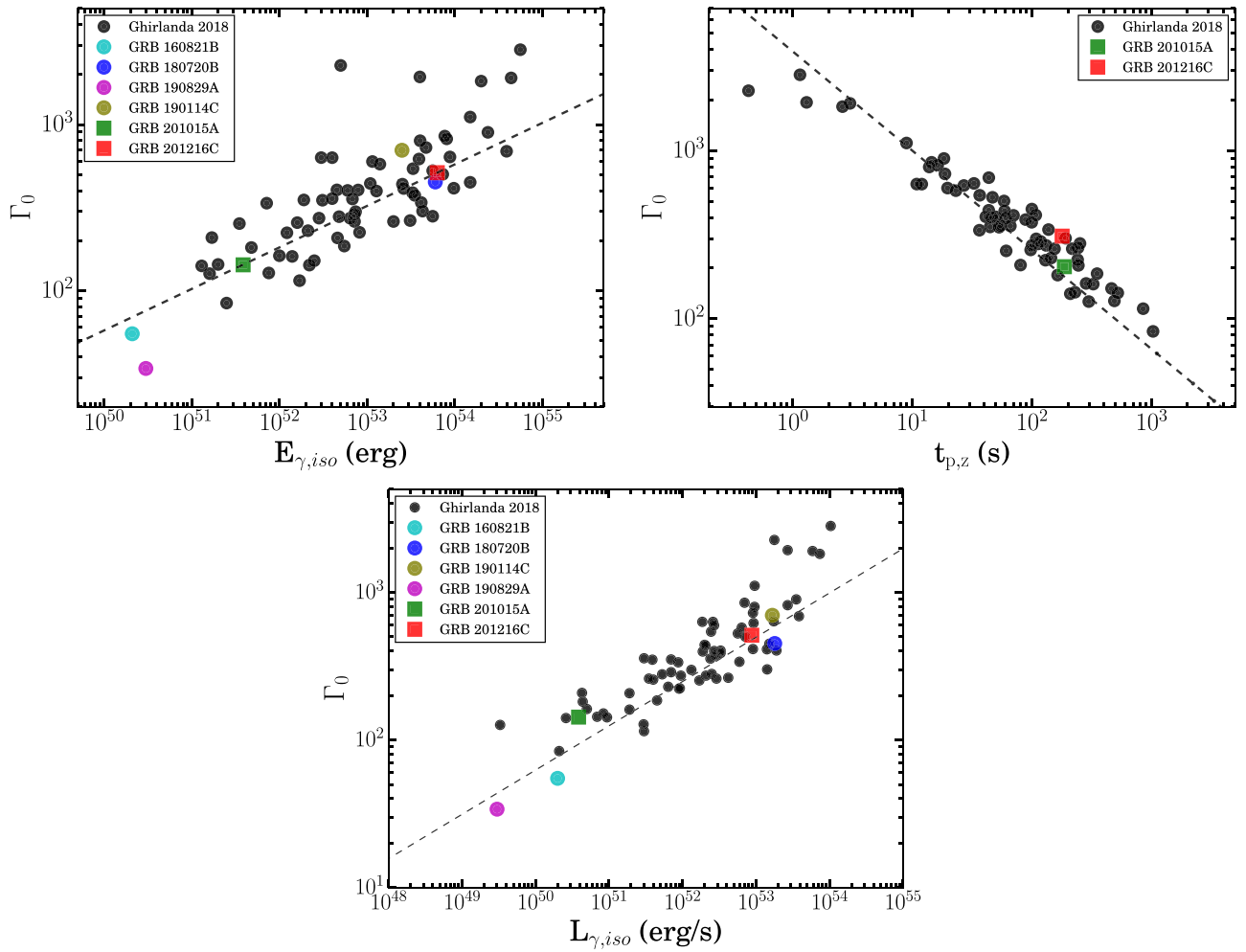


Figure A9. The upper left and right panels represent the two important tight correlations Γ_0 - $E_{\gamma,iso}$ and Γ_0 - $t_{p,z}$, respectively, discovered by the L2010. The lower panel represents the Γ_0 - $L_{\gamma,iso}$ correlation given by Lü et al. (2012). The data points shown with black dots are taken from Ghirlanda et al. (2018). The green and red squares represent GRB 201015A and GRB 201216C, respectively, clearly satisfying the given correlations. The data points shown with various colored dots are taken from the publications cited in Table 1.

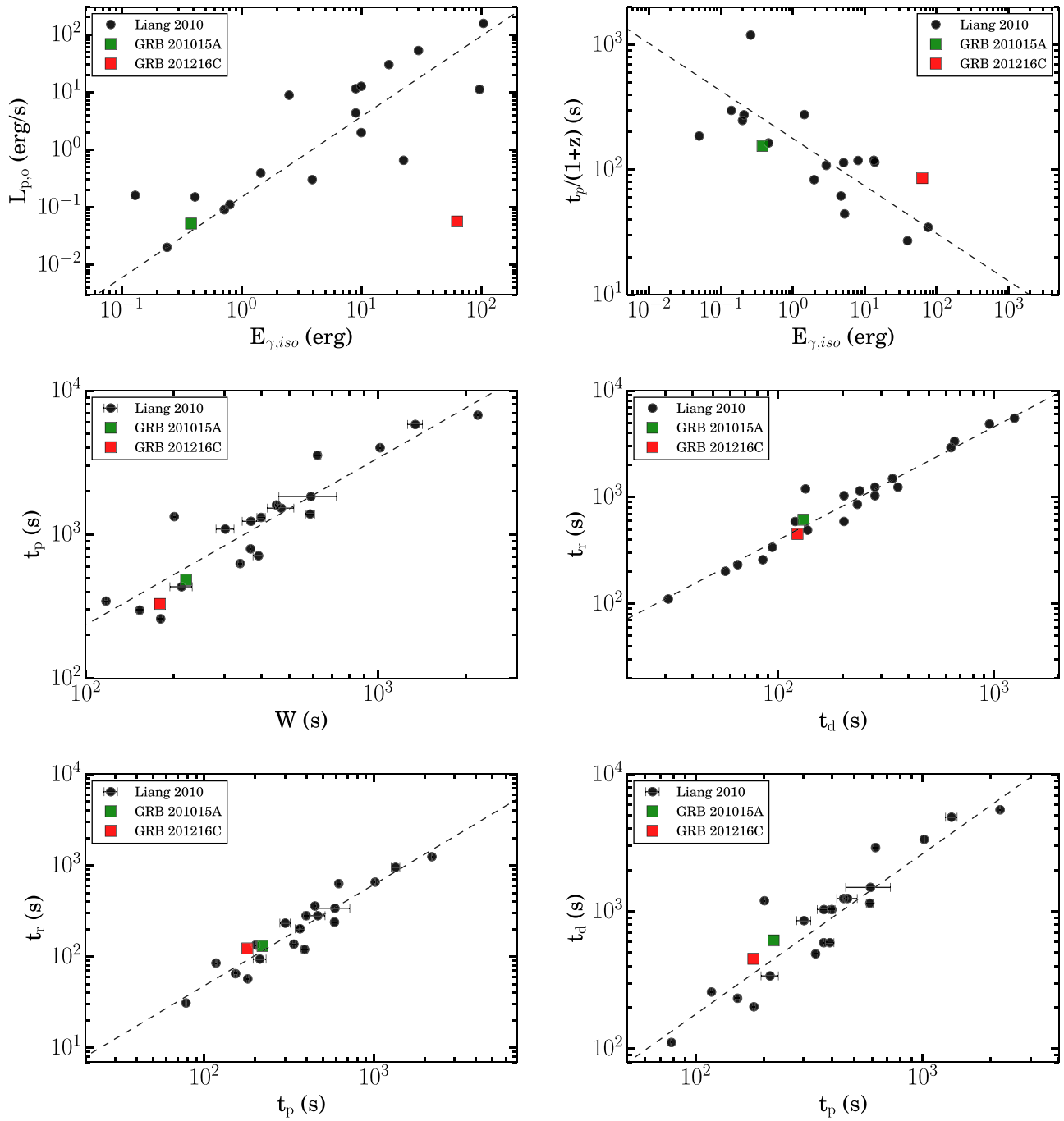


Figure A10. Correlations between the onset parameters studied by the [L2010](#). The green and red squares represent GRB 201015A and GRB 201216C, respectively. GRB 201216C is not satisfying the $L_{p,o}-E_{\gamma,iso}$ correlation, indicating the dark nature of the burst.

Appendix B Additional Tables

Table B1
Results of the Time-averaged ($T_0 - 0.503$ to $T_0 + 47.09$ s) Spectral Fitting of the GBM Data for GRB 201216C

Model	Spectral Parameters					Statistics	
	α_{pt}	E_p / E_c (keV)	β_{pt}	kT_{BB} (keV)	Flux ($\text{erg cm}^{-2} \text{s}^{-1}$)	DIC	Δ DIC
Band	$-1.07^{+0.01}_{-0.01}$	$344.15^{+9.86}_{-9.90}$	$-2.35^{+0.05}_{-0.05}$...	4.29×10^{-06}	7609.74	...
Band+BB	$-0.98^{+0.02}_{-0.02}$	$352.31^{+12.77}_{-12.74}$	$-2.39^{+0.06}_{-0.06}$	$9.94^{+0.52}_{-0.52}$	4.26×10^{-06}	7502.07	-107.67
CPL	$-1.11^{+0.01}_{-0.01}$	$452.95^{+11.52}_{-11.70}$	3.38×10^{-06}	7684.57	...
CPL+BB	$-1.07^{+0.01}_{-0.01}$	$464.40^{+17.94}_{-17.64}$...	$12.63^{+0.86}_{-0.83}$	3.45×10^{-06}	7558.00	-126.57
Synchrotron	B (G)	p	γ_{cool}		Flux ($\text{erg cm}^{-2} \text{s}^{-1}$)	DIC	Δ DIC
	$142.60^{+11.49}_{-11.42}$	$5.02^{+0.60}_{-0.56}$	$180875.73^{+9787.31}_{-10325.27}$...	4.11×10^{-06}	7454.89	...

Note. The time-integrated flux has been calculated in the 10 keV–10 MeV energy range.

Table B2
Time-resolved Spectral Analysis Results of GRB 201216C Modeled by the Empirical Cutoff Power-law (CPL) and CPL + Blackbody Models

$t_{\text{start}}-t_{\text{stop}}$ (s)	S	CPL			CPL+BB				CPL DIC	CPL+BB DIC	Δ DIC
		Γ	E_p (keV)	Flux	α_{pt}	E_p (keV)	kT (keV)	Flux			
3.93–5.68	40.93	$-1.00^{0.05}_{-0.05}$	$483.52^{78.55}_{-77.87}$	2.42×10^6	$-0.94^{0.08}_{-0.08}$	$517.54^{110.79}_{-111.94}$	$14.66^{4.17}_{-3.74}$	2.68×10^6	2394.02	2365.42	-28.6
5.68–6.23	35.83	$-0.98^{0.05}_{-0.05}$	$637.45^{112.58}_{-111.95}$	5.2×10^6	$-0.87^{0.08}_{-0.08}$	$681.70^{139.82}_{-140.22}$	$16.88^{2.87}_{-2.84}$	5.73×10^6	665.66	637.12	-28.54
6.23–7.24	63.53	$-0.89^{0.03}_{-0.03}$	$583.88^{61.08}_{-61.01}$	8.08×10^6	$-0.83^{0.05}_{-0.05}$	$598.39^{83.53}_{-83.68}$	$17.04^{3.38}_{-3.05}$	8.36×10^6	1739.16	1719.61	-19.55
7.24–10.19	120.81	$-0.91^{0.02}_{-0.02}$	$452.07^{23.97}_{-23.52}$	7.21×10^6	$-0.85^{0.04}_{-0.04}$	$460.25^{37.65}_{-37.54}$	$15.52^{2.05}_{-2.06}$	7.43×10^6	3437.91	3396.15	-41.76
10.19–11.02	46.78	$-1.02^{0.05}_{-0.05}$	$333.80^{44.99}_{-46.34}$	3.21×10^6	$-0.94^{0.07}_{-0.07}$	$339.63^{52.78}_{-53.97}$	$12.22^{1.87}_{-1.68}$	3.32×10^6	1256.32	1242.7	-13.63
11.02–14.90	77.15	$-1.08^{0.03}_{-0.03}$	$297.07^{25.32}_{-25.36}$	2.15×10^6	$-1.01^{0.04}_{-0.04}$	$289.91^{27.71}_{-28.00}$	$10.13^{1.12}_{-1.16}$	2.19×10^6	3505.93	3491.02	-14.91
14.90–15.66	48.58	$-1.04^{0.05}_{-0.05}$	$401.31^{57.84}_{-58.67}$	3.92×10^6	$-1.03^{0.07}_{-0.07}$	$443.88^{87.04}_{-89.72}$	$14.13^{5.97}_{-5.39}$	4.21×10^6	1227.59	1214.58	-13.02
15.66–17.28	59.96	$-1.03^{0.04}_{-0.04}$	$251.80^{26.75}_{-26.80}$	2.35×10^6	$-1.03^{0.07}_{-0.07}$	$277.08^{33.24}_{-47.17}$	$12.59^{5.70}_{-4.46}$	2.61×10^6	2286.17	2267.03	-19.14
17.74–18.58	48.27	$-1.17^{0.04}_{-0.04}$	$405.31^{61.81}_{-62.19}$	3.22×10^6	$-1.12^{0.05}_{-0.05}$	$413.46^{65.97}_{-67.32}$	$10.87^{2.11}_{-1.98}$	3.31×10^6	1236.56	1229.42	-7.15
18.58–19.87	73.73	$-1.02^{0.03}_{-0.03}$	$430.15^{39.74}_{-39.88}$	5.27×10^6	$-0.99^{0.04}_{-0.04}$	$439.19^{48.92}_{-49.23}$	$13.13^{3.99}_{-3.47}$	5.44×10^6	2005.36	1995.71	-9.65
19.87–20.47	62.39	$-1.08^{0.03}_{-0.03}$	$587.08^{76.28}_{-76.91}$	7.57×10^6	$-1.06^{0.05}_{-0.05}$	$730.58^{127.50}_{-127.81}$	$18.14^{2.80}_{-2.78}$	8.36×10^6	1052.87	1028.02	-24.85
20.47–21.42	61.86	$-1.08^{0.04}_{-0.04}$	$362.22^{42.79}_{-43.14}$	4.06×10^6	$-1.07^{0.05}_{-0.05}$	$408.69^{69.94}_{-68.74}$	$14.25^{3.71}_{-3.31}$	4.36×10^6	1480.71	1468.67	-12.04
21.42–21.72	44.21	$-1.02^{0.05}_{-0.05}$	$528.13^{82.39}_{-83.90}$	7.55×10^6	$-1.01^{0.05}_{-0.05}$	$566.01^{105.48}_{-106.30}$	$14.49^{7.99}_{-8.60}$	7.95×10^6	13.17	7.63	-5.53
21.72–22.92	61.99	$-1.10^{0.04}_{-0.04}$	$310.73^{33.31}_{-33.62}$	3.25×10^6	$-1.06^{0.05}_{-0.05}$	$313.66^{36.36}_{-36.88}$	$10.56^{1.64}_{-1.58}$	3.28×10^6	1845.48	1837.52	-7.96
22.92–23.85	76.31	$-0.99^{0.03}_{-0.03}$	$387.04^{32.54}_{-32.61}$	6.35×10^6	$-0.95^{0.04}_{-0.04}$	$381.01^{25.02}_{-35.13}$	$11.60^{2.23}_{-2.07}$	6.46×10^6	1581.2	1573.82	-7.38
23.85–24.28	76.51	$-0.93^{0.03}_{-0.03}$	$412.51^{36.40}_{-36.18}$	1.17×10^6	$-0.92^{0.04}_{-0.04}$	$418.79^{38.80}_{-41.01}$	$12.71^{6.72}_{-6.75}$	1.19×10^6	638.32	634.18	-4.14
24.28–24.73	66.46	$-0.97^{0.04}_{-0.04}$	$370.73^{36.53}_{-36.39}$	8.69×10^6	$-0.99^{0.06}_{-0.06}$	$471.95^{81.21}_{-81.47}$	$20.52^{4.20}_{-4.24}$	9.39×10^6	621.01	598.12	-22.88
24.73–25.83	123.46	$-1.05^{0.02}_{-0.02}$	$517.88^{33.69}_{-33.73}$	1.24×10^6	$-1.04^{0.03}_{-0.03}$	$601.55^{66.01}_{-66.48}$	$18.14^{3.10}_{-3.08}$	1.33×10^6	2082.07	2047.75	-34.32
25.83–27.53	134.88	$-1.06^{0.02}_{-0.02}$	$463.91^{26.31}_{-26.29}$	9.58×10^6	$-1.04^{0.03}_{-0.03}$	$467.15^{31.36}_{-34.63}$	$12.74^{2.85}_{-3.14}$	9.92×10^6	2664.38	2650.17	-14.21
27.53–28.15	97.35	$-1.10^{0.02}_{-0.02}$	$579.32^{50.10}_{-50.35}$	1.28×10^6	$-1.09^{0.03}_{-0.03}$	$672.64^{81.84}_{-82.16}$	$18.28^{3.16}_{-3.13}$	1.36×10^6	1248.52	1229.01	-19.51
28.15–29.06	97.18	$-1.19^{0.02}_{-0.02}$	$519.64^{48.03}_{-47.69}$	8.29×10^6	$-1.18^{0.03}_{-0.03}$	$622.46^{77.40}_{-77.14}$	$15.59^{1.93}_{-1.86}$	8.95×10^6	1679.26	1654.19	-25.07
29.06–29.79	69.43	$-1.28^{0.04}_{-0.03}$	$426.52^{58.11}_{-58.70}$	4.71×10^6	$-1.28^{0.04}_{-0.04}$	$558.76^{98.59}_{-99.10}$	$13.60^{1.10}_{-1.12}$	5.06×10^6	1202.71	1182.16	-20.56
29.79–30.81	63.57	$-1.31^{0.04}_{-0.04}$	$407.51^{61.76}_{-61.43}$	3.2×10^6	$-1.30^{0.04}_{-0.04}$	$491.35^{94.87}_{-95.63}$	$12.20^{1.60}_{-1.52}$	3.4×10^6	1659.75	1647.92	-11.83
30.81–31.95	50.74	$-1.39^{0.04}_{-0.04}$	$471.88^{94.56}_{-95.45}$	2.29×10^6	$-1.39^{0.05}_{-0.05}$	$506.05^{113.31}_{-116.77}$	$9.75^{5.23}_{-5.41}$	2.35×10^6	1649.24	1645.29	-3.95
31.95–33.11	39.54	$-1.26^{0.06}_{-0.06}$	$217.73^{37.27}_{-38.05}$	1.34×10^6	$-1.25^{0.07}_{-0.07}$	$262.15^{56.56}_{-58.42}$	$10.61^{1.53}_{-1.44}$	1.43×10^6	1644.47	1635.39	-9.08
33.11–35.71	43.68	$-1.36^{0.05}_{-0.05}$	$288.97^{54.46}_{-55.81}$	1.01×10^6	$-1.39^{0.08}_{-0.08}$	$358.73^{108.86}_{-109.39}$	$11.04^{7.31}_{-6.40}$	1.16×10^6	2812.15	2795.55	-16.6
35.71–38.83	35.6	$-1.36^{0.07}_{-0.07}$	$259.59^{59.37}_{-61.17}$	6.66×10^6	$-1.34^{0.08}_{-0.08}$	$337.47^{103.36}_{-105.31}$	$9.46^{1.37}_{-1.31}$	7.35×10^6	3034.54	3022.18	-12.36

Note. The reported flux values (in $\text{erg cm}^{-2} \text{s}^{-1}$) are calculated in the 10 keV–10 MeV energy range.

Table B3
Time-resolved Spectral Analysis Results of GRB 201216C Modeled by the Empirical Band Function and its Combination using Blackbody (BB) Function

$t_{\text{start}}-t_{\text{stop}}$ (s)	α_{pt}	Band β_{pt}	E_{p} (keV)	Flux	α_{pt}	β_{pt}	Band+BB E_{p} (keV)	kT (keV)	Flux	Band DIC	Band+BB DIC	Δ DIC
3.93–5.68	$-0.97^{0.06}_{-0.06}$	$-2.81^{0.51}_{-0.58}$	$428.87^{65.43}_{-65.55}$	2.78×10^6	$-0.90^{0.10}_{-0.10}$	$-3.02^{0.64}_{-0.69}$	$479.50^{89.10}_{-89.33}$	$13.37^{3.81}_{-3.34}$	2.86×10^6	2391.24	2380.36	-10.88
5.68–6.23	$-0.96^{0.05}_{-0.06}$	$-3.30^{0.44}_{-0.45}$	$606.17^{94.31}_{-93.56}$	5.48×10^6	$-0.85^{0.09}_{-0.09}$	$-3.63^{0.57}_{-0.59}$	$709.63^{121.34}_{-120.59}$	$16.46^{2.91}_{-2.80}$	5.81×10^6	665.42	650.85	-14.57
6.23–7.24	$-0.85^{0.04}_{-0.04}$	$-2.36^{0.16}_{-0.15}$	$562.91^{50.08}_{-50.84}$	1.01×10^5	$-0.77^{0.06}_{-0.06}$	$-2.40^{0.16}_{-0.16}$	$584.21^{56.27}_{-57.14}$	$14.85^{2.73}_{-2.37}$	1.03×10^5	1720.89	1712.18	-8.71
7.24–10.19	$-0.86^{0.02}_{-0.02}$	$-2.39^{0.11}_{-0.11}$	$417.29^{23.51}_{-23.53}$	9.12×10^6	$-0.76^{0.04}_{-0.04}$	$-2.44^{0.12}_{-0.12}$	$432.09^{27.71}_{-27.61}$	$12.66^{1.00}_{-1.01}$	9.03×10^6	3412.17	3384.55	-27.62
10.19–11.02	$-1.01^{0.05}_{-0.05}$	$-3.24^{0.40}_{-0.42}$	$313.48^{29.92}_{-29.52}$	3.46×10^6	$-0.92^{0.07}_{-0.07}$	$-3.43^{0.52}_{-0.55}$	$341.72^{37.28}_{-37.52}$	$12.00^{1.72}_{-1.54}$	3.49×10^6	1254.32	1246.93	-7.39
11.02–14.90	$-1.04^{0.04}_{-0.04}$	$-2.58^{0.29}_{-0.31}$	$239.83^{21.47}_{-21.76}$	2.66×10^6	$-0.97^{0.05}_{-0.05}$	$-2.70^{0.35}_{-0.34}$	$254.91^{23.22}_{-23.81}$	$9.52^{0.99}_{-0.98}$	2.6×10^6	3496.97	3486.73	-10.24
14.90–15.66	$-1.00^{0.06}_{-0.06}$	$-2.65^{0.43}_{-0.47}$	$334.92^{47.49}_{-48.66}$	4.63×10^6	$-0.98^{0.07}_{-0.07}$	$-2.80^{0.52}_{-0.56}$	$372.32^{61.92}_{-65.40}$	$12.24^{5.07}_{-4.88}$	4.75×10^6	1222.70	1218.13	-4.57
15.66–17.28	$-0.95^{0.06}_{-0.06}$	$-2.46^{0.27}_{-0.26}$	$203.28^{22.21}_{-22.37}$	3.13×10^6	$-0.94^{0.07}_{-0.07}$	$-2.56^{0.33}_{-0.32}$	$216.35^{26.31}_{-27.74}$	$9.33^{2.82}_{-3.47}$	3.07×10^6	2277.67	2274.30	-3.37
17.74–18.58	$-1.16^{0.05}_{-0.05}$	$-3.13^{0.48}_{-0.50}$	$324.62^{37.21}_{-37.61}$	3.49×10^6	$-1.11^{0.06}_{-0.06}$	$-3.34^{0.59}_{-0.62}$	$349.90^{43.94}_{-44.38}$	$10.80^{1.99}_{-1.85}$	3.51×10^6	1234.22	1228.86	-5.36
18.58–19.87	$-1.00^{0.04}_{-0.04}$	$-2.55^{0.30}_{-0.30}$	$377.18^{36.48}_{-36.28}$	6.54×10^6	$-0.97^{0.05}_{-0.05}$	$-2.64^{0.35}_{-0.34}$	$397.69^{42.65}_{-43.41}$	$11.92^{3.55}_{-3.25}$	6.53×10^6	1997.41	1992.54	-4.87
19.87–20.47	$-1.00^{0.07}_{-0.07}$	$-2.31^{0.28}_{-0.28}$	$406.97^{86.54}_{-85.82}$	9.79×10^6	$-1.04^{0.06}_{-0.06}$	$-2.93^{0.55}_{-0.60}$	$637.73^{110.37}_{-111.05}$	$17.67^{3.03}_{-3.00}$	9.42×10^6	1042.53	1027.14	-15.39
20.47–21.42	$-1.06^{0.04}_{-0.04}$	$-2.95^{0.44}_{-0.48}$	$307.31^{29.47}_{-29.31}$	4.49×10^6	$-1.05^{0.06}_{-0.06}$	$-3.18^{0.55}_{-0.59}$	$347.84^{43.44}_{-44.89}$	$13.25^{3.62}_{-3.15}$	4.58×10^6	1477.02	1470.68	-6.34
21.42–21.72	$-1.00^{0.06}_{-0.06}$	$-2.56^{0.39}_{-0.43}$	$470.72^{76.95}_{-77.99}$	9.45×10^6	$-1.00^{0.06}_{-0.06}$	$-2.64^{0.43}_{-0.45}$	$521.73^{102.66}_{-103.01}$	$14.10^{8.36}_{-8.48}$	9.79×10^6	7.15	2.77	-4.38
21.72–22.92	$-1.08^{0.04}_{-0.04}$	$-3.04^{0.46}_{-0.51}$	$263.76^{22.36}_{-22.35}$	3.59×10^6	$-1.04^{0.05}_{-0.05}$	$-3.28^{0.61}_{-0.65}$	$281.16^{26.37}_{-26.48}$	$10.34^{1.64}_{-1.54}$	3.56×10^6	1842.93	1836.55	-6.38
22.92–23.85	$-0.98^{0.03}_{-0.03}$	$-3.47^{0.35}_{-0.35}$	$382.29^{24.40}_{-24.00}$	6.69×10^6	$-0.94^{0.04}_{-0.04}$	$-3.78^{0.52}_{-0.53}$	$394.20^{26.52}_{-26.48}$	$11.46^{2.13}_{-1.99}$	6.68×10^6	1580.47	1574.85	-5.62
23.85–24.28	$-0.92^{0.03}_{-0.03}$	$-2.94^{0.36}_{-0.39}$	$417.58^{30.28}_{-29.90}$	1.31×10^5	$-0.91^{0.04}_{-0.04}$	$-3.01^{0.42}_{-0.43}$	$427.04^{33.68}_{-34.54}$	$11.62^{5.38}_{-5.97}$	1.32×10^5	632.94	630.25	-2.69
24.28–24.73	$-0.89^{0.06}_{-0.06}$	$-2.47^{0.26}_{-0.24}$	$313.48^{39.88}_{-39.43}$	1.08×10^5	$-0.95^{0.08}_{-0.08}$	$-2.97^{0.55}_{-0.59}$	$427.92^{74.58}_{-77.28}$	$18.77^{5.09}_{-4.79}$	1.05×10^5	612.58	599.65	-12.92
24.73–25.83	$-0.99^{0.03}_{-0.03}$	$-2.36^{0.11}_{-0.11}$	$402.27^{29.66}_{-29.46}$	1.54×10^5	$-0.98^{0.03}_{-0.04}$	$-2.50^{0.17}_{-0.16}$	$463.80^{43.59}_{-43.91}$	$14.62^{1.97}_{-1.92}$	1.52×10^5	2056.01	2039.19	-16.82
25.83–27.53	$-1.05^{0.02}_{-0.02}$	$-3.08^{0.34}_{-0.37}$	$414.49^{20.77}_{-20.94}$	1.03×10^5	$-1.02^{0.03}_{-0.03}$	$-3.18^{0.41}_{-0.43}$	$422.88^{22.77}_{-23.47}$	$11.33^{1.62}_{-2.08}$	1.03×10^5	2658.61	2651.25	-7.36
27.53–28.15	$-1.07^{0.03}_{-0.03}$	$-2.70^{0.34}_{-0.35}$	$465.77^{48.69}_{-50.77}$	1.47×10^5	$-1.08^{0.04}_{-0.04}$	$-3.11^{0.48}_{-0.52}$	$574.32^{64.04}_{-64.06}$	$17.62^{3.33}_{-3.22}$	1.47×10^5	1241.25	1227.12	-14.13
28.15–29.06	$-1.17^{0.03}_{-0.03}$	$-2.93^{0.48}_{-0.53}$	$388.63^{38.55}_{-39.46}$	9.17×10^6	$-1.18^{0.03}_{-0.03}$	$-3.45^{0.55}_{-0.57}$	$498.32^{51.08}_{-51.01}$	$15.48^{1.90}_{-1.86}$	9.36×10^6	1674.67	1652.97	-21.70
29.06–29.79	$-1.19^{0.08}_{-0.08}$	$-2.41^{0.34}_{-0.39}$	$233.62^{52.59}_{-52.57}$	6.00×10^6	$-1.27^{0.04}_{-0.05}$	$-3.18^{0.63}_{-0.65}$	$387.90^{63.30}_{-63.20}$	$13.51^{1.15}_{-1.15}$	5.5×10^6	1192.50	1179.51	-13.00
29.79–30.81	$-1.21^{0.09}_{-0.09}$	$-2.22^{0.24}_{-0.20}$	$197.90^{47.40}_{-49.75}$	4.63×10^6	$-1.27^{0.06}_{-0.06}$	$-2.60^{0.48}_{-0.55}$	$292.42^{64.36}_{-66.04}$	$11.53^{1.84}_{-1.71}$	4.14×10^6	1645.06	1641.88	-3.18
30.81–31.95	$-1.37^{0.05}_{-0.05}$	$-2.85^{0.55}_{-0.59}$	$262.67^{46.46}_{-46.22}$	2.55×10^6	$-1.38^{0.06}_{-0.06}$	$-3.00^{0.65}_{-0.69}$	$284.65^{56.88}_{-56.64}$	$9.21^{4.86}_{-4.97}$	2.6×10^6	1644.99	1642.27	-2.73
31.95–33.11	$-1.21^{0.08}_{-0.09}$	$-3.06^{0.59}_{-0.58}$	$146.46^{21.30}_{-19.71}$	1.49×10^6	$-1.24^{0.08}_{-0.08}$	$-3.39^{0.62}_{-0.64}$	$187.49^{30.93}_{-31.05}$	$10.51^{1.54}_{-1.44}$	1.52×10^6	1640.42	1635.42	-5.00
33.11–35.71	$-1.31^{0.07}_{-0.07}$	$-2.85^{0.51}_{-0.57}$	$159.75^{23.99}_{-24.54}$	1.15×10^6	$-1.33^{0.08}_{-0.08}$	$-3.05^{0.64}_{-0.69}$	$176.09^{31.61}_{-32.33}$	$8.53^{5.32}_{-4.61}$	1.18×10^6	2808.19	2803.98	-4.21
35.71–38.83	$-1.21^{0.18}_{-0.16}$	$-2.56^{0.51}_{-0.61}$	$122.37^{35.51}_{-40.78}$	8.68×10^7	$-1.29^{0.09}_{-0.10}$	$-3.01^{0.66}_{-0.68}$	$188.78^{44.68}_{-45.08}$	$9.01^{1.39}_{-1.25}$	8.03×10^7	2984.82	3020.93	36.11

Note. The reported flux values (in $\text{erg cm}^{-2} \text{s}^{-1}$) are calculated in the 10 keV–10 MeV energy range.

Table B4
Time-resolved Spectral Analysis Results of GRB 201216C Modeled by the Physical Synchrotron Model

$t_{\text{start}}-t_{\text{stop}}$ (s)	S	Synchrotron				DIC
		B (G)	p	$\gamma_{\text{cool}} \times 10^4$ (keV)	Flux	
3.93–5.68	40.93	127.44 ^{+52.09} _{-57.34}	4.17 ^{+1.17} _{-1.12}	71.28 ^{+14.32} _{-50.33}	3.04×10^6	1061.27
5.68–6.23	35.83	191.76 ^{+62.20} _{-60.38}	4.88 ^{+0.78} _{-0.79}	41.95 ^{+10.09} _{-21.68}	6.07×10^6	495.69
6.23–7.24	63.52	141.95 ^{+76.50} _{-80.01}	3.65 ^{+0.86} _{-0.73}	145.89 ^{+43.00} _{-115.55}	1.06×10^5	268.10
7.24–10.19	120.80	119.98 ^{+26.07} _{-26.00}	4.33 ^{+0.82} _{-0.75}	43.89 ^{+8.73} _{-9.60}	8.87×10^6	3220.77
10.19–11.02	46.78	82.79 ^{+22.44} _{-22.41}	4.74 ^{+0.83} _{-0.82}	39.92 ^{+11.87} _{-15.12}	3.75×10^6	1135.13
11.02–14.90	77.15	66.66 ^{+15.62} _{-15.68}	4.35 ^{+0.95} _{-0.91}	3162 ^{+6.43} _{-7.43}	2.58×10^6	3337.24
14.90–15.66	48.57	83.41 ^{+41.46} _{-45.05}	3.87 ^{+1.17} _{-1.03}	95.85 ^{+22.89} _{-73.26}	4.88×10^6	-1025.49
15.66–17.28	59.95	36.96 ^{+18.32} _{-19.85}	3.78 ^{+0.97} _{-0.78}	163.60 ^{+85.52} _{-126.22}	2.93×10^6	976.25
17.74–18.58	48.27	96.21 ^{+23.76} _{-23.41}	4.48 ^{+0.96} _{-0.93}	21.09 ^{+4.98} _{-5.95}	3.82×10^6	1114.54
18.58–19.87	73.72	102.62 ^{+31.12} _{-31.92}	3.88 ^{+0.99} _{-0.89}	34.08 ^{+8.43} _{-10.35}	6.71×10^6	1662.13
19.87–20.47	62.38	161.77 ^{+55.49} _{-54.98}	4.00 ^{+1.08} _{-1.00}	28.86 ^{+6.06} ₋₁₃	9.67×10^6	-617.38
20.47–21.42	61.86	88.19 ^{+21.46} _{-22.10}	4.54 ^{+0.89} _{-0.87}	28.87 ^{+6.80} _{-8.04}	4.8×10^6	1357.23
21.42–21.72	44.21	118.33 ^{+70.63} _{-75.31}	3.49 ^{+0.99} _{-0.88}	89.76 ^{+30.89} _{-69.89}	1.01×10^5	-1935.17
21.72–22.92	61.99	70.93 ^{+14.80} _{-14.81}	4.57 ^{+0.87} _{-0.85}	29.05 ^{+6.44} _{-6.89}	3.79×10^6	1789.03
22.92–23.85	76.31	102.43 ^{+16.92} _{-16.82}	5.17 ^{+0.60} _{-0.60}	36.06 ^{+6.88} _{-7.11}	7.29×10^6	1566.58
23.85–24.28	76.51	90.59 ^{+29.41} _{-30.21}	4.37 ^{+0.92} _{-0.87}	89.68 ^{+22.42} _{-53.08}	1.38×10^5	262.16
24.28–24.73	66.46	66.04 ^{+31.36} _{-35.67}	3.87 ^{+0.97} _{-0.82}	129.61 ^{+62.92} _{-94.28}	1.06×10^5	-545.52
24.73–25.83	123.46	151.66 ^{+27.59} _{-27.87}	4.44 ^{+0.84} _{-0.79}	23.00 ^{+3.35} _{-3.38}	1.52×10^5	1984.83
25.83–27.53	134.88	141.10 ^{+15.30} _{-15.02}	5.24 ^{+0.55} _{-0.57}	22.36 ^{+2.31} _{-2.35}	1.12×10^5	2643.94
27.53–28.15	97.34	171.33 ^{+33.96} _{-33.88}	4.61 ^{+0.86} _{-0.82}	18.96 ^{+3.10} _{-3.13}	1.55×10^5	1192.78
28.15–29.06	97.18	133.21 ^{+21.71} _{-22.68}	4.70 ^{+0.83} _{-0.80}	15.87 ^{+2.28} _{-2.31}	9.80×10^6	1629.70
29.06–29.79	69.43	63.99 ^{+26.77} _{-27.73}	3.73 ^{+1.18} _{-1.11}	39.21 ^{+7.60} _{-25.50}	5.62×10^6	-6121.04
29.79–30.81	63.56	37.73 ^{+27.24} _{-28.41}	2.93 ^{+0.83} _{-0.72}	90.80 ^{+42.48} _{-75.68}	4.39×10^6	-11527.37
30.81–31.95	50.73	56.91 ^{+15.59} _{-14.74}	3.68 ^{+1.02} _{-0.93}	13.96 ^{+2.77} _{-3.34}	2.62×10^6	1527.57
31.95–33.11	39.54	30.09 ^{+11.61} _{-13.44}	4.17 ^{+1.10} _{-1.09}	87.37 ^{+17.70} _{-67.43}	1.53×10^6	-310.89
33.11–35.71	43.67	38.01 ^{+10.34} _{-10.31}	3.93 ^{+0.89} _{-0.89}	20.75 ^{+5.92} _{-8.47}	1.16×10^6	2521.27
35.71–38.83	35.60	19.82 ^{+15.81} _{-14.46}	3.33 ^{+1.07} _{-0.80}	189.08 ^{+135.21} _{-172.28}	8.61×10^7	-3405.36

Note. The reported flux values (in $\text{erg cm}^{-2} \text{s}^{-1}$) are measured in the 10 keV–10 MeV energy channels.

Table B5
Mean and Standard Deviation of Spectral Parameters of Several Fitting Models Obtained from the Time-resolved Spectral Analysis of GRB 201216C

Model	Spectral Parameters				
	α_{pt}	E_p/E_c (keV)	β_{pt}	kT (keV)	Flux ($\text{erg cm}^{-2} \text{s}^{-1}$)
Band	-1.06 ± 0.13	339.43 ± 119.39	-2.75 ± 0.33	...	$(6.50 \pm 4.08) \times 10^{-06}$
Band+BB	-1.04 ± 0.16	394.54 ± 135.69	-3.01 ± 0.36	12.66 ± 2.76	$(6.48 \pm 4.07) \times 10^{-06}$
CPL	-1.10 ± 0.14	421.77 ± 109.31	$(5.50 \pm 3.45) \times 10^{-06}$
CPL+BB	-1.07 ± 0.16	467.78 ± 126.97	...	13.73 ± 2.92	$(5.81 \pm 3.63) \times 10^{-06}$
Synchrotron	B (G)	p	γ_{cool}	...	Flux ($\text{erg cm}^{-2} \text{s}^{-1}$)
	96.00 ± 45.82	4.18 ± 0.54	608341.26 ± 480884.31	...	$(6.71 \pm 4.21) \times 10^{-06}$

Table B6
Spectral Parameter Correlation Results Obtained using Pearson Correlation

Model	log (Flux)–log (E_p)		log (Flux)– α_{pt}		log (E_p)– α_{pt}		log (Flux)– kT	
	r	p	r	p	r	p	r	p
Band	0.79	7.19×10^{-7}	0.60	9.67×10^{-4}	0.65	2.11×10^{-4}
Band+BB	0.83	7.75×10^{-8}	0.53	4.13×10^{-3}	0.56	2.39×10^{-3}	0.72	2.51×10^{-5}
Synchrotron		log (Flux)–log (B)		log (Flux)– p		log (B)– p		log (B)– p
	r	p	r	p	r	p	r	p
	0.80	5.43×10^{-7}	0.31	1.10×10^{-1}	0.54	3.53×10^{-3}		
		log (E_p)–log (B)		log (B)– α_{pt}		α_{pt} – p		
	r	p	r	p	r	p		
Band–Synchrotron	0.96	5.14×10^{-15}	0.55	3.23×10^{-3}	0.24	2.31×10^{-1}		

Note. r and P denote the Pearson correlation coefficient and the likelihood of a null hypothesis, respectively.

Table B7
Magnitudes of 13 Secondary Standard Stars in the Vicinity of GRB 201015A, Calibrated against the Landolt Standard Field PG 0231

ID	U	B	V	R	I
1	17.75 ± 0.14	16.81 ± 0.02	15.63 ± 0.00	14.94 ± 0.01	14.29 ± 0.04
2	17.58 ± 0.14	17.19 ± 0.02	16.34 ± 0.01	15.82 ± 0.01	15.35 ± 0.04
3	17.95 ± 0.14	17.72 ± 0.02	17.00 ± 0.01	16.55 ± 0.01	16.14 ± 0.04
4	18.46 ± 0.14	18.06 ± 0.02	17.19 ± 0.01	16.66 ± 0.01	16.14 ± 0.04
5	17.50 ± 0.14	17.28 ± 0.02	16.59 ± 0.01	16.15 ± 0.01	15.75 ± 0.04
6	17.16 ± 0.14	16.79 ± 0.02	16.00 ± 0.01	15.53 ± 0.01	15.10 ± 0.04
7	18.11 ± 0.14	17.86 ± 0.02	17.06 ± 0.01	16.55 ± 0.01	16.11 ± 0.04
8	18.30 ± 0.14	17.76 ± 0.02	16.89 ± 0.01	16.34 ± 0.01	15.86 ± 0.04
9	17.18 ± 0.14	16.77 ± 0.02	15.94 ± 0.01	15.43 ± 0.01	14.98 ± 0.04
10	17.79 ± 0.14	17.40 ± 0.02	16.54 ± 0.01	16.02 ± 0.01	15.55 ± 0.04
11	15.90 ± 0.14	15.69 ± 0.02	15.07 ± 0.00	14.69 ± 0.01	14.36 ± 0.04
12	18.25 ± 0.14	16.60 ± 0.02	15.14 ± 0.00	14.33 ± 0.01	13.54 ± 0.04
13	17.83 ± 0.14	17.49 ± 0.02	16.63 ± 0.01	16.04 ± 0.01	15.49 ± 0.04

Note. Observations were obtained using the $4K \times 4K$ CCD Imager (Kumar et al. 2022b), the first light instrument on the axial port of 3.6 m DOT.

Table B8
Optical Afterglow Observations of GRB 201015A

Time (s)	Exp Time (s)	Filter	Telescope	Magnitude	References
46.65	20	C	FRAM-ORM	17.49 ± 0.19	Present work
72.57	20	C	FRAM-ORM	17.71 ± 0.22	Present work
100.22	20	C	FRAM-ORM	17.61 ± 0.20	Present work
126.14	20	C	FRAM-ORM	17.37 ± 0.18	Present work
152.92	20	C	FRAM-ORM	16.86 ± 0.10	Present work
178.84	20	C	FRAM-ORM	16.73 ± 0.09	Present work
204.76	20	C	FRAM-ORM	16.67 ± 0.09	Present work
230.68	20	C	FRAM-ORM	16.72 ± 0.09	Present work
256.60	20	C	FRAM-ORM	16.73 ± 0.10	Present work
283.39	20	C	FRAM-ORM	16.96 ± 0.12	Present work
309.31	20	C	FRAM-ORM	16.74 ± 0.10	Present work
335.23	20	C	FRAM-ORM	16.63 ± 0.09	Present work
361.15	20	C	FRAM-ORM	16.90 ± 0.11	Present work
387.07	20	C	FRAM-ORM	16.67 ± 0.09	Present work
412.99	20	C	FRAM-ORM	16.79 ± 0.10	Present work
438.91	20	C	FRAM-ORM	16.77 ± 0.11	Present work
464.83	20	C	FRAM-ORM	16.75 ± 0.10	Present work
490.75	20	C	FRAM-ORM	16.93 ± 0.12	Present work
516.67	20	C	FRAM-ORM	17.01 ± 0.13	Present work
542.59	20	C	FRAM-ORM	17.09 ± 0.14	Present work
605.66	98	C	FRAM-ORM	17.40 ± 0.09	Present work
709.34	98	C	FRAM-ORM	17.64 ± 0.09	Present work
813.88	98	C	FRAM-ORM	17.65 ± 0.09	Present work

Table B8
(Continued)

Time (s)	Exp Time (s)	Filter	Telescope	Magnitude	References
917.56	98	<i>C</i>	FRAM-ORM	17.95 ± 0.12	Present work
1022.11	98	<i>C</i>	FRAM-ORM	18.19 ± 0.15	Present work
40.60	11	<i>C</i>	BOOTES-1B	17.49 ± 0.47	Present work
103.68	30	<i>C</i>	BOOTES-1B	17.68 ± 0.52	Present work
162.43	15	<i>C</i>	BOOTES-1B	16.59 ± 0.29	Present work
194.40	10	<i>C</i>	BOOTES-1B	16.41 ± 0.35	Present work
221.18	10	<i>C</i>	BOOTES-1B	16.58 ± 0.38	Present work
247.10	10	<i>C</i>	BOOTES-1B	16.54 ± 0.37	Present work
273.88	10	<i>C</i>	BOOTES-1B	16.20 ± 0.30	Present work
304.12	14	<i>C</i>	BOOTES-1B	17.04 ± 0.49	Present work
329.18	10	<i>C</i>	BOOTES-1B	16.96 ± 0.31	Present work
340.41	10	<i>C</i>	BOOTES-1B	16.69 ± 0.25	Present work
351.64	10	<i>C</i>	BOOTES-1B	16.71 ± 0.25	Present work
362.88	10	<i>C</i>	BOOTES-1B	17.12 ± 0.34	Present work
374.97	10	<i>C</i>	BOOTES-1B	17.09 ± 0.32	Present work
386.20	10	<i>C</i>	BOOTES-1B	16.55 ± 0.23	Present work
398.30	10	<i>C</i>	BOOTES-1B	16.57 ± 0.23	Present work
408.67	10	<i>C</i>	BOOTES-1B	16.97 ± 0.29	Present work
420.76	10	<i>C</i>	BOOTES-1B	16.89 ± 0.28	Present work
432.00	10	<i>C</i>	BOOTES-1B	17.07 ± 0.34	Present work
444.09	10	<i>C</i>	BOOTES-1B	16.78 ± 0.26	Present work
455.32	10	<i>C</i>	BOOTES-1B	17.09 ± 0.33	Present work
467.42	10	<i>C</i>	BOOTES-1B	17.19 ± 0.36	Present work
477.79	10	<i>C</i>	BOOTES-1B	16.90 ± 0.28	Present work
500.25	30	<i>C</i>	BOOTES-1B	18.20 ± 0.64	Present work
535.68	30	<i>C</i>	BOOTES-1B	17.39 ± 0.30	Present work
569.37	30	<i>C</i>	BOOTES-1B	16.98 ± 0.23	Present work
604.80	30	<i>C</i>	BOOTES-1B	16.99 ± 0.24	Present work
650.59	50	<i>C</i>	BOOTES-1B	17.51 ± 0.29	Present work
707.61	50	<i>C</i>	BOOTES-1B	17.07 ± 0.22	Present work
764.64	50	<i>C</i>	BOOTES-1B	17.50 ± 0.29	Present work
851.90	100	<i>C</i>	BOOTES-1B	17.75 ± 0.27	Present work
966.81	100	<i>C</i>	BOOTES-1B	17.70 ± 0.28	Present work
1080.86	100	<i>C</i>	BOOTES-1B	17.87 ± 0.30	Present work
1195.77	100	<i>C</i>	BOOTES-1B	17.89 ± 0.31	Present work
1368.57	200	<i>C</i>	BOOTES-1B	18.22 ± 0.50	Present work
1656.28	300	<i>C</i>	BOOTES-1B	18.08 ± 0.21	Present work
2016.57	300	<i>C</i>	BOOTES-1B	18.60 ± 0.26	Present work
2399.32	300	<i>C</i>	BOOTES-1B	18.72 ± 0.16	Present work
2928.09	600	<i>C</i>	BOOTES-1B	19.24 ± 0.21	Present work
3889.72	900	<i>C</i>	BOOTES-1B	19.01 ± 0.24	Present work
5011.20	900	<i>C</i>	BOOTES-1B	19.92 ± 0.32	Present work
6096.38	840	<i>C</i>	BOOTES-1B	19.63 ± 0.27	Present work
72316.80	300	<i>I</i>	DOT	21.88 ± 0.09	Present work
52099.20	300	<i>R</i>	DOT	22.14 ± 0.08	Present work
73008.00	300	<i>R</i>	DOT	21.94 ± 0.12	Present work
52790.40	300	<i>V</i>	DOT	22.70 ± 0.08	Present work
73267.20	300	<i>V</i>	DOT	22.63 ± 0.09	Present work
74217.60	300	<i>B</i>	DOT	23.31 ± 0.10	Present work

Note. The quoted magnitude values are in the AB system and are not corrected for foreground extinction.

Table B9
Our Optical Afterglow Observations of GRB 201216C with FRAM-ORM

time (s)	Exposure (s)	Filter	Telescope	Magnitude	References
47.410	20	<i>C</i>	FRAM-ORM	18.339 ± 0.295	Present work
73.770	20	<i>C</i>	FRAM-ORM	>18.38	Present work
112.40	45	<i>C</i>	FRAM-ORM	19.101 ± 0.421	Present work
154.26	20	<i>C</i>	FRAM-ORM	18.036 ± 0.251	Present work
180.23	20	<i>C</i>	FRAM-ORM	18.034 ± 0.253	Present work
218.19	46	<i>C</i>	FRAM-ORM	18.269 ± 0.252	Present work
293.39	98	<i>C</i>	FRAM-ORM	18.563 ± 0.247	Present work
398.52	98	<i>C</i>	FRAM-ORM	18.775 ± 0.299	Present work
526.91	150	<i>C</i>	FRAM-ORM	18.665 ± 0.239	Present work
813.95	467	<i>C</i>	FRAM-ORM	19.226 ± 0.227	Present work
1643.47	21×60	<i>R</i>	FRAM-ORM	19.927 ± 0.346	Present work
7884.00	3×40	<i>r</i>	VLT	21.81 ± 0.05	Izzo et al. (2020)

Note. The quoted magnitude values are in the AB system and are not corrected for foreground extinction.

Table B10

Closure Relations Obtained from the Best-fit Values of the Spectral and Temporal Indices for GRB 201015A and GRB 201216C using Swift-XRT and our Optical Observations from FRAM-ORM, BOOTES, and 3.6 m DOT

GRB 201015A							
Time Interval (s)	α_o	α_x	β_o	β_x	p	Spectral Regime	Medium
3300–4800	$-0.92^{+0.08}_{-0.09}$	$-2.36^{+0.17}_{-0.26}$...	$-1.07^{+0.31}_{-0.30}$	2.72 ± 0.44	$\nu_m < \nu_o < \nu_c < \nu_x$	ISM
$(1.0\text{--}180) \times 10^4$	$-0.92^{+0.08}_{-0.09}$	$-2.36^{+0.17}_{-0.26}$	$-1.13^{+0.30}_{-0.30}$	$-1.38^{+0.49}_{-0.47}$	2.93 ± 0.38	$\nu_m < \nu_o < \nu_c < \nu_x$	ISM
GRB 201216C							
Time interval (s)	α_o	α_x	β_o	β_x	p	Spectral regime	Medium
2900–17,000	$-1.05^{+0.11}_{-0.10}$	$-2.21^{+0.10}_{-0.11}$...	$-0.97^{+0.05}_{-0.05}$	2.42 ± 0.48	$\nu_m < \nu_o < \nu_c < \nu_x$	wind

ORCID iDs

Amit Kumar Ror  <https://orcid.org/0000-0003-3164-8056>
 Martin Jelínek  <https://orcid.org/0000-0003-3922-7416>
 Y.-D. Hu  <https://orcid.org/0000-0002-7400-4608>
 Alžběta Maleňáková  <https://orcid.org/0000-0002-0636-9138>
 Jan Štrobl  <https://orcid.org/0000-0002-4147-2878>
 Christina C. Thöne  <https://orcid.org/0000-0002-7978-7648>
 Sergey Karpov  <https://orcid.org/0000-0003-0035-651X>
 Amit Kumar  <https://orcid.org/0000-0002-4870-9436>
 A. Aryan  <https://orcid.org/0000-0002-9928-0369>
 M. D. Caballero-García  <https://orcid.org/0000-0001-7920-4564>
 A. Castellón  <https://orcid.org/0000-0003-4646-0451>

References

Abbott, B. P., Abbott, R., Abbott, T. D., et al. 2017, *ApJL*, **848**, L13
 Abdalla, H., Adam, R., Aharonian, F., et al. 2019, *Natur*, **575**, 464
 Ahumada, T., Singer, L. P., Anand, S., et al. 2021, *NatAs*, **5**, 917
 Amati, L. 2006, *MNRAS*, **372**, 233
 Arnaud, K. A. 1996, in ASP Conf. Ser. 101, *Astronomical Data Analysis Software and Systems V*, ed. G. H. Jacoby & J. Barnes (San Francisco, CA: ASP), 17
 Astropy Collaboration, Robitaille, T. P., Tollerud, E. J., et al. 2013, *A&A*, **558**, A33
 Band, D., Matteson, J., Ford, L., et al. 1993, *ApJ*, **413**, 281
 Barthelmy, S. D., Barbier, L. M., Cummings, J. R., et al. 2005, *SSRv*, **120**, 143
 Beardmore, A. P., Gropp, J. D., Kennea, J. A., et al. 2020, *GCN*, **29061**, 1

Becker, A. 2015, HOTPANTS: High Order Transform of PSF ANd Template Subtraction, Astrophysics Source Code Library, ascl:1504.004
 Bissaldi, E., Omodei, N., Kocevski, D., et al. 2020, *GCN*, **29076**, 1
 Blandford, R. D., & McKee, C. F. 1976, *PhFl*, **19**, 1130
 Bromberg, O., Nakar, E., & Piran, T. 2011, *ApJL*, **739**, L55
 Burgess, J. M. 2014, *MNRAS*, **445**, 2589
 Burgess, J. M., Bégué, D., Greiner, J., et al. 2020, *NatAs*, **4**, 174
 Burrows, D. N., Hill, J. E., Nousek, J. A., et al. 2005, *SSRv*, **120**, 165
 Caballero-García, M. D., Gupta, R., Pandey, S. B., et al. 2022, *MNRAS*, in press
 Campana, S., Cusumano, G., Evans, P. A., et al. 2020, *GCN*, **29064**, 1
 Chand, V., Banerjee, A., Gupta, R., et al. 2020, *ApJ*, **898**, 42
 de Ugarte Postigo, A., Kann, D. A., Blazek, M., et al. 2020a, *GCN*, **28649**, 1
 de Ugarte Postigo, A., Thöne, C. C., Martín, S., et al. 2020b, *A&A*, **633**, A68
 de Ugarte Postigo, A., et al. 2022, *GCN*, **32648**, 1
 D’Elia, V., Ambrosi, E., Barthelmy, S. D., et al. 2020, *GCN*, **28632**, 1
 Dichiaro, S., Gropp, J. D., Kennea, J. A., et al. 2022, *GCN*, **32632**, 1
 Evans, P. A., Beardmore, A. P., Page, K. L., et al. 2007, *A&A*, **469**, 379
 Evans, P. A., Beardmore, A. P., Page, K. L., et al. 2009, *MNRAS*, **397**, 1177
 Fong, W., Berger, E., Margutti, R., & Zauderer, B. A. 2015, *ApJ*, **815**, 102
 Fraija, N., Dichiaro, S., Pedreira, A. C. C. d. E. S., et al. 2019a, *ApJL*, **879**, L26
 Fraija, N., Dichiaro, S., Pedreira, A. C. C. d. E. S., et al. 2019b, *ApJ*, **885**, 29
 Fraija, N., Veres, P., Beniamini, P., et al. 2021, *ApJ*, **918**, 12
 Frederiks, D., Golenetskii, S., Aptekar, R., et al. 2020, *GCN*, **29084**, 1
 Fukami, S., Berti, A., Loporchio, S., et al. 2022, *Proc. ICRC (Berlin)*, **37**, 788
 Gao, H., Wang, X.-G., Mészáros, P., & Zhang, B. 2015, *ApJ*, **810**, 160
 Gao, H.-X., Geng, J.-J., & Huang, Y.-F. 2021, *A&A*, **656**, A134
 Ghirlanda, G., Nappo, F., Ghisellini, G., et al. 2018, *A&A*, **609**, A112
 Giarratana, S., Rhodes, L., Marcote, B., et al. 2022, *A&A*, **664**, A36
 Goldstein, A., Veres, P., Burns, E., et al. 2017, *ApJL*, **848**, L14
 Golenetskii, S. V., Mazets, E. P., Aptekar, R. L., & Ilinskii, V. N. 1983, *Natur*, **306**, 451
 Golkhou, V. Z., Butler, N. R., & Littlejohns, O. M. 2015, *ApJ*, **811**, 93

- Gupta, R., Bhushan Pandey, S., Kumar, A., et al. 2022a, *ApA*, 43, 82
- Gupta, R., Gupta, S., Chattopadhyay, T., et al. 2022b, *MNRAS*, 511, 1694
- Gupta, R., Kumar, A., Pandey, S. B., et al. 2022c, *JApA*, 43, 11
- Gupta, R., Oates, S. R., Pandey, S. B., et al. 2021a, *MNRAS*, 505, 4086
- Gupta, R., Pandey, S. B., Castro-Tirado, A. J., et al. 2021b, *RMxAC*, 53, 113
- H.E.S.S. Collaboration, Abdalla, H., Aharonian, F., et al. 2021, *Sci*, 372, 1081
- Hjorth, J., Sollerman, J., Møller, P., et al. 2003, *Natur*, 423, 847
- Hu, Y. D., Castro-Tirado, A. J., Kumar, A., et al. 2021, *A&A*, 646, A50
- Hu, Y. D., Fernandez-Garcia, E., Castro-Tirado, A. J., et al. 2020, *GCN*, 28645, 1
- Huang, X.-L., Liang, E.-W., Liu, R.-Y., Cheng, J.-G., & Wang, X.-Y. 2020, *ApJL*, 903, L26
- Huang, Y., Hu, S., Chen, S., et al. 2022, *GCN*, 32677, 1
- Hunter, J. D. 2007, *CSE*, 9, 90
- Izzo, L., Malesani, D. B., & Kann, D. A. 2020, *GCN*, 29066, 1
- Jelinek, M., Strobl, J., Karpov, S., et al. 2020a, *GCN*, 28664, 1
- Jelinek, M., Strobl, J., Karpov, S., et al. 2020b, *GCN*, 29070, 1
- Jordana-Mitjans, N., Mundell, C. G., Kobayashi, S., et al. 2020, *ApJ*, 892, 97
- Kargatis, V. E., Liang, E. P., Hurley, K. C., et al. 1994, *ApJ*, 422, 260
- Kennea, J. A., Tagliaferri, G., Campana, S., et al. 2020, *GCN*, 28635, 1
- Kobayashi, S., & Zhang, B. 2003, *ApJL*, 582, L75
- Kouveliotou, C., Meegan, C. A., Fishman, G. J., et al. 1993, *ApJL*, 413, L101
- Kumar, A., Pandey, S. B., Gupta, R., et al. 2022a, *NewA*, 97, 101889
- Kumar, A., Pandey, S. B., Singh, A., et al. 2022b, *JApA*, 43, 27
- Kumar, P., & Zhang, B. 2015, *PhR*, 561, 1
- Lamb, G. P., Tanvir, N. R., Levan, A. J., et al. 2019, *ApJ*, 883, 48
- Li, L., Geng, J.-J., Meng, Y.-Z., et al. 2019, *ApJ*, 884, 109
- Liang, E.-W., Yi, S.-X., Zhang, J., et al. 2010, *ApJ*, 725, 2209
- Lin, D.-B., Lu, R.-J., Du, S.-S., et al. 2019, *ApJ*, 883, 187
- Lipunov, V., Gorbvskoy, E., Kornilov, V., et al. 2020, *GCN*, 28633, 1
- Lü, H.-J., Yuan, H.-Y., Yi, T.-F., et al. 2022, *ApJL*, 931, L23
- Lü, J., Zou, Y.-C., Lei, W.-H., et al. 2012, *ApJ*, 751, 49
- MAGIC Collaboration, Acciari, V. A., Ansoldi, S., et al. 2019a, *Natur*, 575, 455
- MAGIC Collaboration, Acciari, V. A., Ansoldi, S., et al. 2019b, *Natur*, 575, 459
- Malacaria, C., Veres, P., Meegan, C., Bissaldi, E. & Fermi GBM Team 2020, *GCN*, 29073, 1
- Malesani, D. B., de Ugarte Postigo, A., & Pursimo, T. 2020, *GCN*, 28637, 1
- Markwardt, C. B., Barthelmy, S. D., Cummings, J. R., et al. 2020, *GCN*, 28658, 1
- Meegan, C., Lichti, G., Bhat, P., et al. 2009, *ApJ*, 702, 791
- Minaev, P. Y., & Pozanenko, A. S. 2020, *MNRAS*, 492, 1919
- Misra, K., Resmi, L., Kann, D. A., et al. 2021, *MNRAS*, 504, 5685
- Molinari, E., Vergani, S. D., Malesani, D., et al. 2007, *A&A*, 469, L13
- Nadella, D., Waratkar, G., Vibhute, A., et al. 2020, *GCN*, 29074, 1
- Nava, L. 2021, *Univ*, 7, 503
- Nava, L., Salvaterra, R., Ghirlanda, G., et al. 2012, *MNRAS*, 421, 1256
- Noda, K., & Parsons, R. D. 2022, *Galax*, 10, 7
- Norris, J. P., Share, G. H., Messina, D. C., et al. 1986, *ApJ*, 301, 213
- Oganesyan, G., Nava, L., Ghirlanda, G., Melandri, A., & Celotti, A. 2019, *A&A*, 628, A59
- Pe'er, A. 2015, *AdAst*, 2015, 907321
- Perna, R., & Belczynski, K. 2002, *ApJ*, 570, 252
- Preece, R. D., Briggs, M. S., Mallozzi, R. S., et al. 2000, *ApJS*, 126, 19
- Rastinejad, J. C., Gompertz, B. P., Levan, A. J., et al. 2022, *Natur*, 612, 223
- Ren, J., Wang, Y., & Zhang, L.-L. 2022, arXiv:2210.10673
- Rhodes, L., van der Horst, A. J., Fender, R., et al. 2022, *MNRAS*, 513, 1895
- Ryde, F., Yu, H.-F., Dereli-Bégué, H., et al. 2019, *MNRAS*, 484, 1912
- Sari, R., & Piran, T. 1999, *ApJ*, 520, 641
- Sari, R., Piran, T., & Narayan, R. 1998, *ApJL*, 497, L17
- Sato, Y., Obayashi, K., Theodre Zhang, B., et al. 2022, arXiv:2208.13987
- Scargle, J. D., Norris, J. P., Jackson, B., & Chiang, J. 2013, *ApJ*, 764, 167
- Shemi, A., & Piran, T. 1990, *ApJL*, 365, L55
- Stetson, P. B. 1987, *PASP*, 99, 191
- Suda, Y., Artero, M., Asano, K., et al. 2022, *Proc. ICRC (Berlin)*, 37, 797
- Tody, D. 1986, *Proc. SPIE*, 627, 733
- Tody, D. 1993, in ASP Conf. Ser. 52, *Astronomical Data Analysis Software and Systems II*, ed. R. J. Hanisch, R. J. V. Brissenden, & J. Barnes (San Francisco, CA: ASP), 173
- Troja, E., Castro-Tirado, A. J., Becerra González, J., et al. 2019, *MNRAS*, 489, 2104
- Troja, E., Fryer, C. L., O'Connor, B., et al. 2022, *Natur*, 612, 228
- Ukwatta, T. N., Barthelmy, S. D., Beardmore, A. P., et al. 2020, *GCN*, 29080, 1
- Vianello, G. 2018, *ApJS*, 236, 17
- Vianello, G., Gill, R., Granot, J., et al. 2018, *ApJ*, 864, 163
- Vianello, G., Lauer, R. J., Younk, P., et al. 2015, arXiv:1507.08343
- Vielfaure, J. B., Izzo, L., Xu, D., et al. 2020, *GCN*, 29077, 1
- Vinko, J., & Wheeler, J. C. 2022, *ATel*, 15712, 1
- Willingale, R., Starling, R. L. C., Beardmore, A. P., Tanvir, N. R., & O'Brien, P. T. 2013, *MNRAS*, 431, 394
- Woosley, S. E. 1993, *ApJ*, 405, 273
- Yonetoku, D., Murakami, T., Nakamura, T., et al. 2004, *ApJ*, 609, 935
- Zhang, B., & Zhang, B. 2014, *ApJ*, 782, 92
- Zhang, B. B., Zhang, B., Castro-Tirado, A. J., et al. 2018, *NatAs*, 2, 69
- Zhang, L.-L., Ren, J., Huang, X.-L., et al. 2021, *ApJ*, 917, 95
- Zhang, Z. B., Jiang, M., Zhang, Y., et al. 2020, *ApJ*, 902, 40